UiT The Arctic University of Norway

UNIS The University Centre in Svalbard

Faculty of Science and Technology
Department of Physics and Technology

On the Distribution of Meteoric Smoke Particles above Andøya, Norway, and Estimated Collection During a Summer Rocket Campaign

Herman Larsen Greaker

FYS-3931 Master's thesis in Space Physics - December 2023

Abstract

As meteoroids enter the Earth's atmosphere, the majority will fully evaporate in the altitude region 70–110 km, due to the frictional heating from atmospheric interactions. The evaporated material is thought to re-condense and coagulate into nanometer sized particles called meteoric smoke particles (MSP). These particles are thought to be a central component in the formation of noctilucent clouds and polar mesospheric summer echoes. In an effort to further investigate and prove the existence of MSPs, the University in Tromsø have designed the MEteoric Smoke Sampler (MESS) instrument. MESS will be mounted on the MAXIDUSTY-2 (MXD2) sounding rocket, scheduled to launch from Andøya, Norway (69.3°N 16°E) in the summer of 2025.

This thesis investigates the expected mesospheric MSP conditions during the possible launch months of the MXD2 rocket. By using the results from a combination of the Whole Atmosphere Community Climate Model (WACCM) and the Community Aerosol and Radiation Model (CARMA), we attempt to investigate the monthly and yearly variations in MSP densities for June, July and August. The WACCM/CARMA model is developed by the University of Leeds, and models the global atmospheric transportation of MSPs based on a yearly meteoric source function. Our analysis considers MSP sizes in the range 1–10 nm, as these are the lower limit of sizes expected to be collected by MESS. Additionally, we present an estimate for the amount of collected MSPs with MESS for a sampling area from 80 to 95 km.

The results showed that despite the general transportation of MSPs away from the summer pole, the June mesopause appeared to possess the highest mesospheric MSP densities throughout the year. Along with the potential of ice particle layers, this suggests June as a feasible month for the MXD2 rocket campaign. The MSP collection estimates showed a density on the order of $10^7\ /cm^2$ on the collection surface of MESS. This result does not consider the additional mass collected through mesospheric ice particles.

Acknowledgements

First and foremost I would like to thank my main supervisor Professor Ingrid Mann for the support and feedback throughout the last year. You have always answered my questions and valued my opinions, to which I am grateful for. A special thank you to my co-supervisor Professor Noora Partamies. Thank you for always having your door open for small and big questions, and the guidance you have given me. I am thankful that you said yes to be my UNIS supervisor. Thank you to Dr Tinna Gunnarsdottir and Dr Wuhu Feng for providing the model data used in this thesis.

To my friends in the masters hallway and the printer room, I am forever thankful for the tremendous fun and motivation you have given me. None of this would be the same without you, thank you all.

Lastly, a thousand thank you to Amalie for keeping me on my feet, and tolerating my hogwash these past years. The support you have given is invaluable. Thank you.

Contents

Abstract iii

Acknowledgements v

List of Figures ix

List of Tables xiii

1 Introduction 1

2 Background 5
2.1 Earth's atmosphere 5
2.2 Stratospheric and mesospheric circulation patterns 6
2.3 Mesospheric smoke particles 11
2.3.1 Formation of meteoric smoke particles 14

3 MAXIDUSTY-2 Rocket Campaign 15
3.1 Mission concept 15
3.1.1 DUSTY 16
3.1.2 MUDD 17
3.1.3 SPID 18
3.1.4 CONE 18
3.1.5 m-NLP and Faraday rotation experiment 19
3.1.6 MAGIC 19
3.2 MESS 20

4 Method 23
4.1 WACCM/CARMA model description 23
4.2 Unit transformations 25
4.3 MSP variations analysis 28
4.4 MSP collection with MESS 29

5 Results and Discussion 33
5.1 Monthly variation in MSPs 33

5.1.1 Discussion 37
5.2 Year-to-year variation in MSPs 37
5.2.1 Discussion 38
5.3 MSP collection estimates with MESS 41
5.3.1 Discussion 44

6 Conclusion **47**

Bibliography **49**

7 Appendix **57**

List of Figures

2.1 Mid-latitudes electron densities profiles for daytime and nighttime during solar maximum and minimum. Adopted from Brekke [2012] 7
2.2 North-south displaced chain of fluid parcels with induced vorticity field (arrows). Thick black line shows the original position of the perturbation. Lighter black line shows the westward displacement of the perturbation due to the advection in the induced vorticity field. The rotational axis of the sphere is given by Ω. Adopted from Holton [2004] 8
2.3 Illustration of the residual mean north-south circulations in the stratosphere and mesosphere. The dark gray ellipses marked R and G, denote the region where Rossby and gravity waves break, driving the Brewer-Dobson circulation and mesospheric meridional circulation. 11
2.4 Illustration showing the formation and transportation of meteoric material within the Earth's atmosphere. The red arrow indicates the meteors' ablation process, and the blue arrow indicates the transport of material. Reprinted from Baumann [2016] 12
2.5 Two dimensional model simulation of global transportation of meteoric material. The contours illustrate the total number density in cm^{-3}. Reprinted from Megner et al. [2008] 13
2.6 Modeled altitude profiles of electrons, positive and negative ions, and positive, negative and neutral MSPs. Reprinted from Baumann et al. [2013] 14

3.1 Schematic illustration of DUSTY [Havnes et al., 1996] 16
3.2 Schematic illustration of MUDD [Antonsen et al., 2017] . . . 17
3.3 Schematic render of SPID [Trollvik et al., 2019] 18
3.4 Current configuration of the MXD2 payload consisting of DUSTY (1), MUDD (2), SPID(3), MAGIC (4), MESS(5), CONE (6), Faraday rotation experiment (7), m-NLP(8). Reprinted from Mann et al. [2022]. 20

3.5 A sliced view of MESS, showing the funnel shape and the sampling surface (1) and reference surface (2). (3) indicate two pressure sensors, and (4) shows the open pressure valve. Figure provided by Sveinung V. Olsen. 21
3.6 Current design of MESS in the open configuration. Figure provided by Sveinung V. Olsen. 22

4.1 Number density and mass density results for MSP bigger than 1 nm from simulation 4 by Bardeen et al. [2008]. The initial MSP size is 0.2 nm with a source function of 16 kt yr^{-1}. Reprinted from Bardeen et al. [2008] 26
4.2 Total number density in January for model years 1 to 22, with years 1, 2 and 3 highlighted in blue, orange and red respectively. Years 4 to 22 are displayed in a diffuse gray color. The model grid point is 69.9°N 19.2°E. 27
4.3 Yearly mean of the total MSP number density from the WACCM/CARMA model N_D, shown together with the approximation to the total MSP number densities as a sum of each MSP size intervals ΣN_r (left), and the difference between them (right). Note the different scales on the horizontal axis. . . . 28

5.1 Monthly averaged MSP density throughout the last model year for particle radius from 1.008 to 8.063 nm. Winter months are shown as dotted lines. Note the different scales on the horizontal axis. 34
5.2 Monthly averaged MSP density between 80 and 90km for particle radius from 1.008 to 8.063 nm. The potential months for the MXD2 rocket campaign is marked. Note the different horizontal scales. The three top and three bottom figures share horizontal axis such that the variation between sizes are clearer. 36
5.3 Total particle concentration for sizes from 1.008 to 8.063 nm over the last twenty model years (year 3 to 22). The Red dashed line shows the average particle concentration over the twenty years. Gray lines shows the individual yearly profiles. 38
5.4 Similar to Figure 5.3 but limited to altitudes from 80 to 90 km and a logarithmic horizontal axis. 39
5.5 Similar results to Figure 5.4 presented in mass density and only for July. 40
5.6 Estimates of the cumulative amount of sampled pure meteoric smoke particles for sampling attempts during June with the MESS instrument. We assume that MESS starts its sampling process at 80 km and end at 95 km. The collection efficiency is fixed at 100% throughout the sampling period. 42

5.7 Estimates of the cumulative amount of sampled MSP for sampling attempts with the MESS instrument during a June campaign. We assume that MESS starts its sampling process at 80 km with a rocket speed of v_r = 1000 and 800 m.s^{-1} 43
5.8 Estimates for the cumulative amount of collected mass for MSP sizes between 1 and 10 nm. The profiles are the same as Figure 5.8 but in the unit of atomic mass unit per square centimeter. 45

List of Tables

4.1 Output parameters from the WACCM/CARMA model simulation. Cumulative over all size bins indicates that the parameter can be regarded as a total, and are not available for each individual size bin. 25
4.2 Collection efficiencies for MESS with a rocket speed 800 $m.s^{-1}$ between 80 and 90 km as found by Pineau et al. [2023]. . . 31
4.3 Collection efficiencies for MESS with a rocket speed 1000 $m.s^{-1}$ between 80 and 90 km as found by Pineau et al. [2023]. 31

1 Introduction

A continuous influx of meteoroids bombards Earth's atmosphere at all times. A fraction of the meteoroids entering the atmosphere ablate in the altitude region 70–110 km. In this region the atmospheric density is high enough for the meteors to be heated to vaporization temperatures. Most meteors fully evaporate and never collide with Earth's surface. The evaporated material is thought to undergo re-condensation and coagulation, giving rise to nanometer sized dust particles [Hunten et al., 1980], so-called meteoric smoke particles (MSP).

The mesospheric dynamics is largely governed by global circulation patterns, connecting the polar regions together in seasonally varying processes. Both mesospheric and stratospheric circulation patterns contribute to making the polar summer mesopause the coldest place in Earth's atmosphere. The low pressure together with the cold temperatures allow for the little water vapour in the mesosphere to freeze dry and form ice particles. Generally, mesospheric constituents are transported away from the summer pole to the winter pole. Thus, MSPs is generally transported away from the summer pole and into the winter pole. The residual MSPs in the summer pole are thought to act as condensation nuclei for the ice particles found in the mesosphere. Mesospheric ice particles can be observed in phenomenas like noctilucent clouds (NLC) [Gadsen and Schroder, 1989] and polar mesospheric summer echoes (PMSE) [Rapp and Lübken, 2004]. Additionally, both MSPs and ice particles have a direct influence on the charge balance of the mesosphere [Baumann et al., 2013].

Remote sensing techniques with satellites [Hervig et al., 2009, 2021], radars and lidars [Plane et al., 2014] are feasible methods for investigating the meso-

sphere. However, remote sensing techniques generally have a low altitude resolution, and limited detection capabilities regarding MSP sizes. An alternative method for investigating mesospheric particles are through rocket mounted instruments [Havnes et al., 1996, 2015, Gunnarsdottir, 2019, Rapp et al., 2005]. Such instruments often provide measurements on electrically charged MSPs, which allows several characteristics of MSPs to be estimated. However, this covers only charged MSPs and depends on assumed charging properties.

Another potential method for investigating MSPs are by sample collection. Several attempts have been made to retrieve MSP samples through rocket mounted instruments in an effort to verify the existence, altitude and size distribution, composition and morphological structure of MSPs [Hedin et al., 2014]. However, there have been no successful attempts at collecting and retrieving MSPs from the mesosphere. The small size and low density of MSPs have proven to be a challenging aspect in previous collection attempts. A better understanding of the size distributions and variations in MSP densities can support the design and planing of future MSP collection attempts.

The most utilized MSP collection instrument is the Mesospheric Aerosol–Genesis, Interaction and Composition (MAGIC) [Hedin et al., 2014]. From 2005 to 2011 MAGIC participated in six different sounding rocket campaigns, both during summer and winter conditions. The speculated reasons for the apparent lack of success in collecting MSPs is aerodynamic filtering and uncertainty in the sticking efficiency of MSP on the collection surface. In an attempt at reducing aerodynamic effects, the University in Tromsø (UiT) has developed the MEteoric Smoke Sampler (MESS). MESS is designed to sample both MSP embedded ice particles and pure MSP. It is expected to be launched on the MAXIDUSTY-2 (MXD2) sounding rocket from Andøya Space (69.3°N 16°E) in the summer of 2025 [Mann et al., 2022]. The sounding rocket includes other dust detectors and in-situ instruments, and will be supported by ground-based instrumentation, such as lidars and radars.

The goal of this thesis is to estimate the expected MSP density conditions during the planned MXD2 rocket launch, based on data from an aerosol and global circulation climate model. We present monthly and yearly variations of MSP number densities at an altitude between 80 and 90 km, as well as estimates for the amount of particles that can be expected to be collected by the MESS instrument during certain conditions. Based on these results we offer a suggestion for which month the MXD2 campaign should take place from a perspective on the collection of pure MSP with MESS. Additionally, we offer a suggestion for which altitude region MESS should operate, in an attempt to optimize the amount of collected MSPs.

The remaining text is structured as followed. Chapter 2 presents a short summary of Earth's atmospheric structure, circulation patterns and MSPs in the mesosphere. This chapter should provide the reader with an overview of the current understanding of MSPs and how they are transported around the upper atmosphere. In chapter 3 we continue with an overview of the MXD2

campaign and the instruments onboard the payload, with a focus on MESS. Chapter 4 presents the simulation model from which results have been used in this thesis. The chapter also explains how we extracted and processed the data. Chapter 5 presents the results from our analysis and discusses them. Chapter 6 contains the conclusion of the thesis, with suggestions for the MXD2 rocket campaign and further research. Lastly, Chapter 7 is the appendix which contains the Python code for the calculations done in this thesis.

2 Background

In this chapter we provide a short overview of Earth's atmosphere, followed by a more in depth explanation of the dynamics of the stratospheric and mesospheric circulation patterns. We consider the physics behind Rossby and gravity waves, and their role in the circulation systems. Lastly, we present an overview of MSPs origin, its interactions with the mesosphere and related atmospheric phenomenas.

2.1 Earth's atmosphere

The Earth's atmosphere is classified according to the horizontal stratification of temperatures. The lowermost region, the troposphere, is where most of the weather related phenomenas occur. Heavy convection and circulation dominates the region, resulting in a tropopause around 10km above the poles, and almost 20km around the equator. The temperature in the troposphere is controlled by the intense solar radiation heating the ground. This results in a vertical decrease in the temperature until the tropopause.

Above the tropopause we find the stratosphere, which contains most of Earth's ozone. The UV absorption by ozone gives rise to an increase in temperature. The name stratosphere indicate that the region is stably stratified with warmer air above colder air. The temperature increase with altitude until the stratopause, which is located at around 50km above the ground. At the altitude from 50km to around 85–90km, we find the mesosphere. The rarefied air is

radiatively cooled causing a negative temperature gradient with altitude. At the mesopause is where we find the coldest region in Earth's atmosphere.

Finally, the thermosphere stretches to an altitude of around 600km. The large mean free path and absorption of high energy solar radiation in this region leads to a positive vertical temperature gradient again. The regions between around 60 to 1000km is collectively called the ionosphere. Here the ionisation of atmospheric constituents becomes highly relevant and free electrons and ions prevail. The ionosphere can be structured into layers according to the variations in electron density. The E-region ranges from around 90km to 150km altitude. With the discovery of its ability to reflect transmitted radio waves due to an electrically conducting layer, it was appropriately named the E-region. Due to the solar activity and the day-night cycles, the ionosphere is highly variable and the exact extent of the E-region is flexible. Further ionospheric research gave rise to the conveniently named D-, F_1- and F_2- regions located below and above the E-region respectively (Figure 2.1).

2.2 Stratospheric and mesospheric circulation patterns

An air parcel located in the Earth's atmosphere is considered to be in an inertial frame of reference compared to Earth's rotating frame of reference. This means that the air parcel is subjected to the inertial forces so-called the Coriolis force and centripetal forces. The centripetal acceleration acting on the air parcel, given as $\vec{\Omega} \times (\vec{\Omega} \times \vec{r})$, will always act from position $\vec{r}$ towards the rotation axis. Here, $\vec{\Omega}$ is the angular velocity of the rotating frame and $\vec{r}$ is the displacement of the air parcel from the axis of rotation. The Coriolis acceleration is given by $2\vec{\Omega} \times \vec{u}$, where $\vec{u}$ is the velocity of the parcel relative to the rotating frame. The Coriolis force will then act perpendicular to the air parcels velocity. The horizontal component is $\Omega u \sin(\phi)$, where ϕ is the latitude. Thus, an air parcel in the northern hemisphere will experience a Coriolis acceleration to the right of its direction of travel, and respectively to the left in the southern hemisphere. From this we can also see that the further north-south of the equator the parcel moves, the stronger is the influence from the Coriolis force.

The winter polar region consists of cold, low-pressure air compared to the subpolar regions. This leads to a pressure gradient directed towards the pole. As the parcel flows from the high pressure area to the low pressure, the Coriolis force will deflect the parcel into an eastward circulating motion around the low pressure area. The summer pole will exhibit a similar vortex around its high pressure area where the Coriolis force is now directed poleward, which creates a westward directed flow. Ideally the pressure force will be in a geostrophic

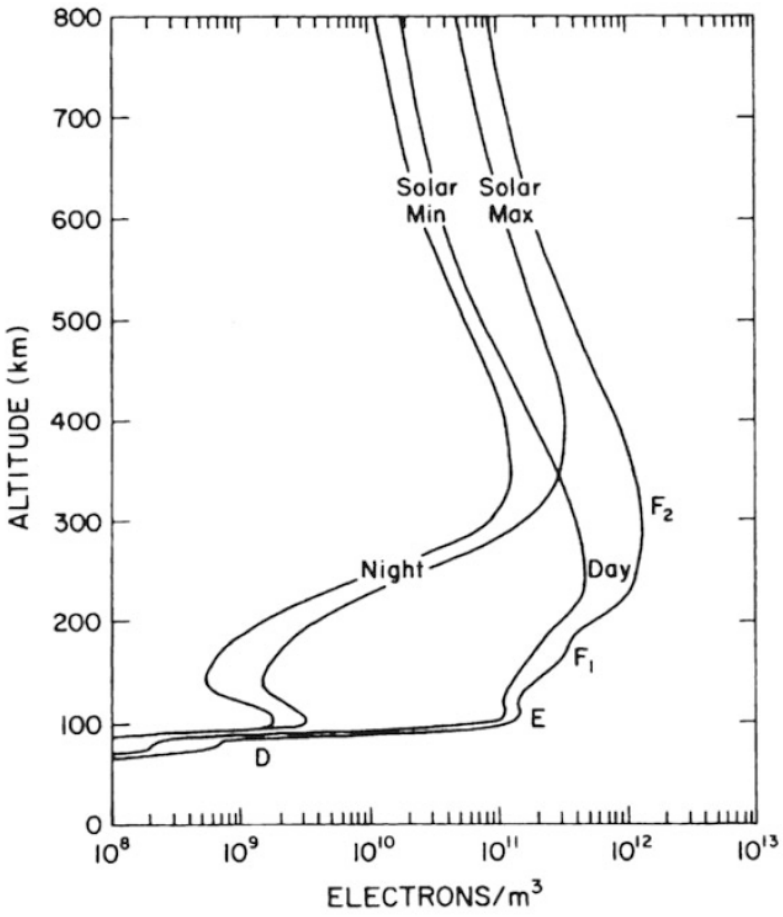

Figure 2.1: Mid-latitudes electron densities profiles for daytime and nighttime during solar maximum and minimum. Adopted from Brekke [2012]

balance with the Coriolis force, sustaining a stable vortex around the polar regions called the polar vortices.

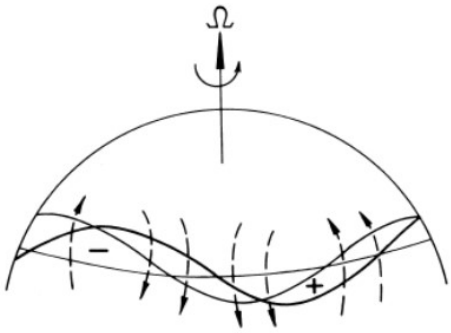

Figure 2.2: North-south displaced chain of fluid parcels with induced vorticity field (arrows). Thick black line shows the original position of the perturbation. Lighter black line shows the westward displacement of the perturbation due to the advection in the induced vorticity field. The rotational axis of the sphere is given by Ω. Adopted from Holton [2004]

Rossby waves (planetary waves) are a result of the meridional variation in the Coriolis force, and the fact that the total vorticity column is a conserved quantity. A series of fluid parcels located at the equator under absolute vorticity conservation will experience no acceleration from the Coriolis force. A northward displacement of the fluid parcels will induce a westward(negative) vorticity, and equally an eastward (positive) vorticity for a southward displacement. Due to the conservation of absolute vorticity, the parcel will resist the meridional displacement, and the parcel will be pulled back towards its equilibrium latitude. The induced vorticity field will advect the parcels southward west of the vorticity minimum and likewise northward west of the vorticity maxima. The resulting perturbation is north-south oscillations of fluid parcels propagating westward as shown in Figure 2.2.

The most influential Rossby waves regarding planetary atmospheric circulation and transportation processes are so-called forced topographic Rossby waves. These are waves excited by topographic features and differential heating over for example land-sea crossings. As described by Charney and Drazin [1961], Rossby waves can only propagate vertically in weak eastward background flows relative to their zonal phase speed. Typically, these waves are excited by geographically locked features, which would cause their zonal phase speed to be zero relative to the ground. Thus, forced topographic Rossby waves will only propagate upwards in eastward directed background wind flows. This special property of Rossby waves allow them to propagate further into the atmosphere during winter, when the previously mentioned polar vortex circulates eastward. Due to energy conservation, when the waves reach the stratosphere's thinner

air, their amplitude grow and they eventually break. The breaking of the waves deposits momentum in the direction of their phase speed relative to the background flow, described through the Eliassen–Palm flux [Holton, 2004]. The westward directed momentum will disrupt the eastward flowing polar vortex in a region named the "surf zone" [Shepherd, 2007]. Due to the conservation of potential vorticity, a poleward flow is set up to restore the geostrophic balance [Plumb, 2002]. This flow is the main transport flow of the Brewer-Dobson circulation, a central part of the tropospheric-stratospheric circulation system [Brewer, 1949, Roscoe, 2006]. For a detailed explanation on the induced poleward flow due to wave breaking we reference Plumb [2002] and Holton [2004]. The Brewer-Dobson circulation transports tropospheric ozone rich air more actively towards the stratospheric winter pole, explaining the high amount of ozone at high latitudes [Dobson and Massey, 1956]. As the tropical ozone rich air descend at the winter polar region, it is compressed [Zhang and Tian, 2019]. The increased pressure and heat from the compression leads to a smaller pressure gradient [Karlsson and Shepherd, 2018]. It follows that the poleward flow decrease and the polar winter vortex is weakened.

Another type of atmospheric waves, important for the middle atmosphere circulation patterns, are those traditionally called gravity waves or buoyancy waves. During a stably stratified atmosphere, a vertically upwards displaced air parcel will be pulled back towards its equilibrium position by gravity. The inertia of the air parcel will cause it to overshoot its equilibrium. The upwards pressure gradient force experienced by the parcel will try to restore the equilibrium again. This continued oscillation is what is known as buoyancy frequency or the Brunt–Väisälä frequency [Nappo, 2002]. Wind flows over topographical features, convective motion, thunderstorms and volcanic eruptions are some events that typically excite gravity waves. In bound fluid systems, like the ocean, buoyancy waves are usually reflected at the boundaries, forming standing waves propagating in the horizontal direction. In the atmospheric system there is no upper boundary, and the waves can propagate vertically upwards as well as horizontal. Such waves are called internal gravity waves [Holton, 2004]. Due to varying sources, gravity waves are excited with a wide spectrum of frequencies and phase speeds. Just like Rossby waves, the amplitude of gravity waves grow as they propagate into the middle atmosphere. As the waves propagate through a horizontal background wind, their intrinsic frequency may be shifted through doppler shifting [Heale and Snively, 2015]. The dispersion relation for internal gravity waves propagation only in x, z plane with the intrinsic frequency ω (Equation 2.1) [Andrews, 2000].

$$\omega^2 = \frac{N^2 k^2}{m^2} \tag{2.1}$$

where N is the buoyancy frequency and k and m are horizontal and vertical

wave number respectively. Expressing 2.1 in terms of the vertical wave number with a shift in intrinsic frequency due to background wind speed u, we get

$$m = \pm \frac{Nk}{(c-u)k} \tag{2.2}$$

Here c is the wave phase speed. From 2.2 we see that if the frequency $\omega = (c-u)k$ is shifted towards the buoyancy frequency, the vertical wave number goes to zero. If the frequency is shifted towards zero i.e., the background wind speed is similar to the phase speed ($u = c$), the vertical wave number grows towards infinity and the wave eventually breaks [Heale and Snively, 2015]. With the wide spectrum of phase speeds in the excited gravity waves, it is not an uncommon occurrence that atmospheric winds match the waves phase speed and the waves undergoes so-called critical-level filtering. A strong homogenous wind as for example the polar vortex may act as a filter, only allowing a certain type of gravity waves to propagate through.

During the eastward directed winter polar vortex, mostly westward propagating gravity waves make it to the mesosphere. The waves eventually break and deposit momentum westward. The coriolis force then induce a poleward flow, similar to the previously mentioned stratospheric circulations induced by Rossby waves. In the summer hemisphere the case is reversed and the breaking of gravity waves induce an equatorward flow. A mesospheric meridional circulation connects the mesospheric summer pole to the winter pole. In Figure 2.3 we show our simplified illustration of the discussed wind flow patterns.

As air is transported to the winter pole by the Brewer-Dobson circulation and the mesospheric meridional circulation, it is compressed and adiabatically heated. The adiabatic heating at the winter pole implies an adiabatic cooling at the summer pole, connected through the mesospheric meridional flow. The cooling of the summer mesosphere results in one of the coldest places in the Earth's atmosphere with temperatures below $120K$ [Sheese et al., 2011, Bailey et al., 2021].

In summary, the forcing from the breaking Rossby waves induce a poleward flow, adiabatically heating the winter pole. This controls the strength of the polar vortex, which in turn control the amount of gravity wave forcing in the mesosphere, again inducing a poleward flow. The adiabatic cooling of the summer polar region resulting from the meridional flows counterintuitively cools the summer polar mesosphere to extreme temperatures, allowing the scarce and dry air to freeze dry and form water ice particles.

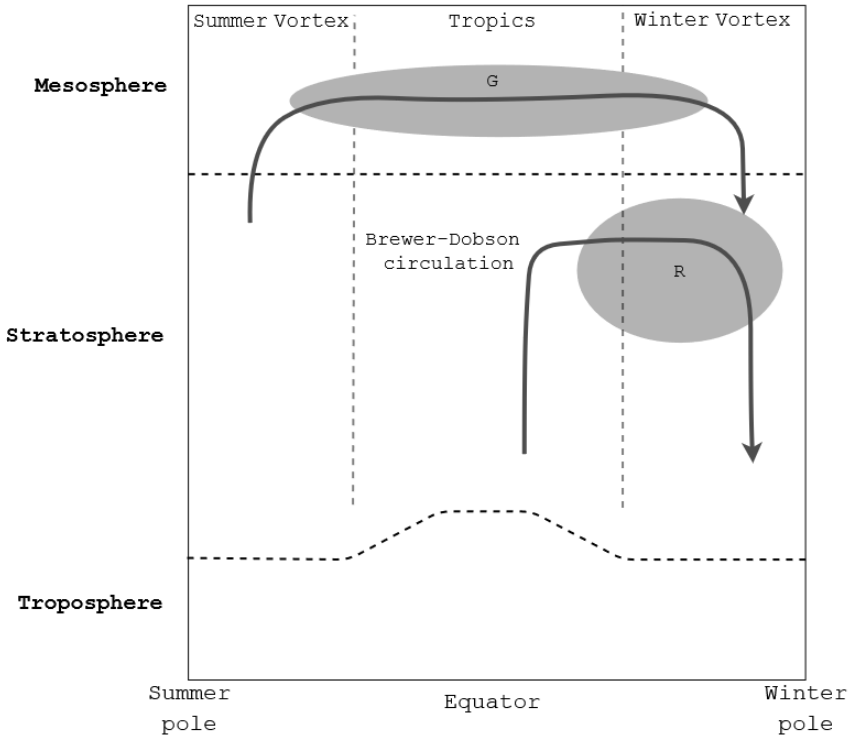

Figure 2.3: Illustration of the residual mean north-south circulations in the stratosphere and mesosphere. The dark gray ellipses marked R and G, denote the region where Rossby and gravity waves break, driving the Brewer-Dobson circulation and mesospheric meridional circulation.

2.3 Mesospheric smoke particles

The Earth is at all times subject to meteoroid bombardment from intersecting comet and asteroid remnants. Estimates for the actual mass influx of extraterrestrial material into Earth's atmosphere range from around 10 to several 100 metric tons a day [Love and Brownlee, 1993, Nesvorný et al., 2009]. Interplanetary dust sourced from the asteroid belt, sublimation of comets passing the sun and dust trails from comets intersecting Earth's orbit are the main source of meteoric mass [Plane, 2012]. A steady rain of meteors with radii from around 5 to 250 μm are the main contributions to the mass influx [Hervig et al., 2009]. As meteors ablate and vaporize in the region 75–110 km of altitude, so-called meteoric smoke or dust particles are formed. The previously discussed wind flows generally transport meteoric particles from the summer mesosphere, to the winter mesosphere [Baumann, 2016, Megner et al., 2008]. Figure 2.4 shows a schematic illustration of the ablation and transportation of meteoric material

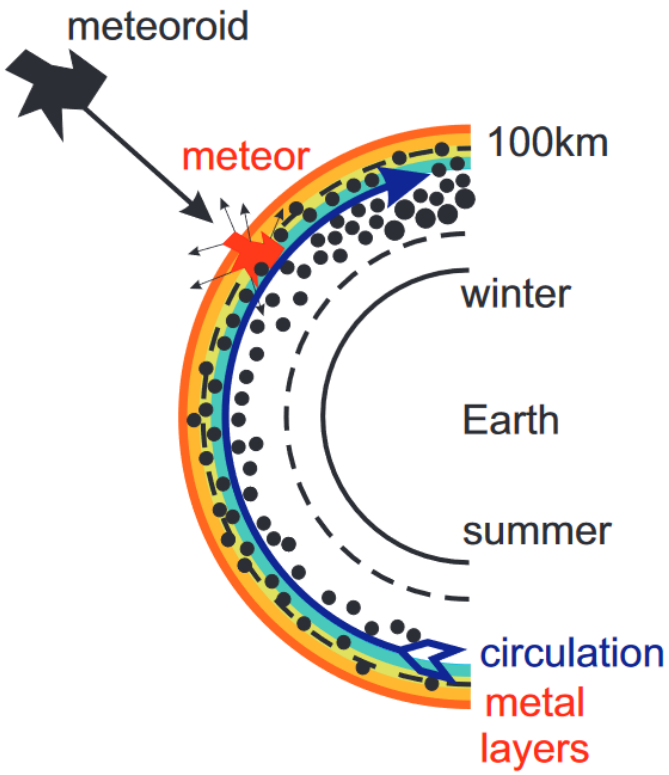

Figure 2.4: Illustration showing the formation and transportation of meteoric material within the Earth's atmosphere. The red arrow indicates the meteors' ablation process, and the blue arrow indicates the transport of material. Reprinted from Baumann [2016]

in the upper atmosphere, and Figure 2.5 shows a numerical model simulation of number densities for different times of the year. It is apparent from Figure 2.5 that the winter stratosphere contains a higher meteoric particle density than the summer stratosphere, showing a clear effect of the atmospheric circulations on the global meteoric material distribution.

As previously mentioned, the summer polar mesosphere is cold enough for the air to freeze dry and form water ice particles. These ice particles are related to phenomenas like NLC and PMSE. NLC are optically observed cloud-like formations resulting from scattering of sun-light from mesospheric ice particles at altitudes around 82 to 85 km. During similar conditions, PMSE can be observed as strong radar echoes in the same altitude region. PMSE and NLC are believed to be associated and contain similar water ice particles [Kassa et al., 2012]. It is thought that meteoric originating smoke particles deposited in the mesosphere are a central part in the nucleation of these ice particles.

Both smoke and ice particles may be charged through processes like the photoelectric effect and plasma attachment [Baumann et al., 2013], such that

they may interact with the ambient plasma. Baumann et al. [2013] did a model study of the D-region charge balance while including the effects of dust/smoke particles, using the Sodankylä Ion and Neutral Chemistry (SIC) model. Figure 2.6 shows a result of the nighttime altitude profiles of plasma components and MSPs modeled above Andøya (69.3°N 16°E) the 8th of September. It is apparent that both charged and neutral particles are a substantial part of the mesospheric constituents and play an important part in the mesospheric charge balance.

As smoke particles are generally transported away from the summer mesosphere, it gives little time for ice particles to nucleate. However, the charge of the particles may significantly contribute to the nucleation process by altering the efficiency of the smoke particles as condensation nuclei, making smoke particles a possible nuclei for mesospheric ice particles [Megner and Gumbel, 2009].

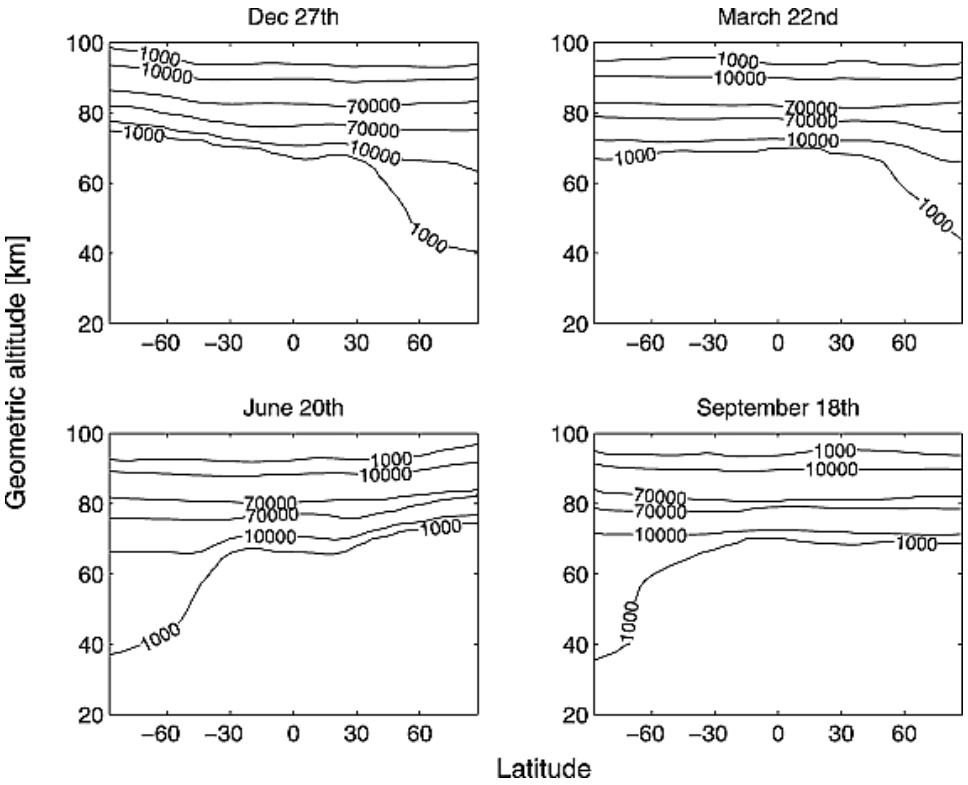

Figure 2.5: Two dimensional model simulation of global transportation of meteoric material. The contours illustrate the total number density in cm^{-3}. Reprinted from Megner et al. [2008]

2.3.1 Formation of meteoric smoke particles

When meteoroids enter the upper mesosphere-lower thermosphere (MLT) region they are heated due to atmospheric friction and start to ablate. The amount of meteoric material deposited during the ablation depends on the size, velocity and composition of the inbound meteors. Generally faster meteoroids, entering the MLT region, ablate at higher altitudes. Considering the extremes, slower and bigger meteoroids may not fully ablate, and deposit less material in the atmosphere. Smaller meteoroids are more efficient at radiating the generated heat and may even be too small($<11.5\mu g$) to experience any evaporation, and thus impacting the Earth's surface fully intact [Megner et al., 2006]. The evaporated material is thought to undergo re-condensation and coagulation with atmospheric constituents into nanometer sized smoke particles [Plane et al., 2014, Hunten et al., 1980].

According to Plane [2012], the current assumptions for the composition of meteoroids is that it consists mainly of magnesium (Mg), silicon (Si) and iron (Fe). The subsequent gas phase transition during ablation is thought to result in compounds in the form of oxides, hydroxides and carbonates of these materials [Plane et al., 2015, Plane, 2003]. Further coagulation occurs as the smoke particles are subjected to sublimation, advection and diffusion during its transportation through the atmosphere [Megner et al., 2006].

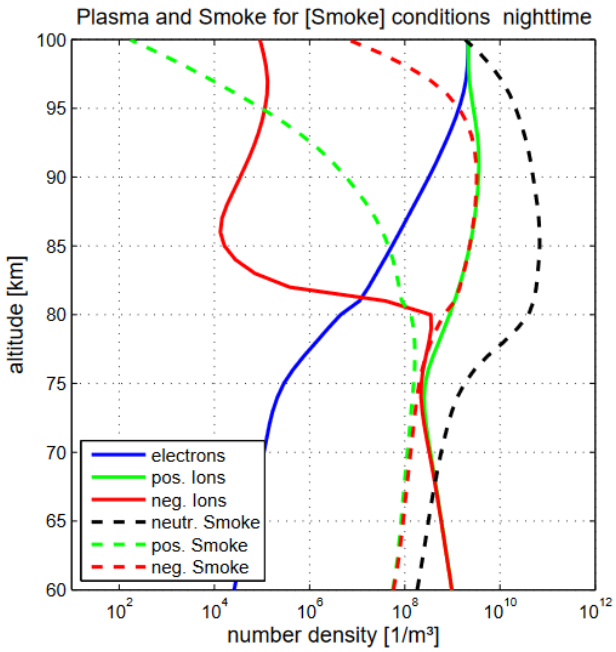

Figure 2.6: Modeled altitude profiles of electrons, positive and negative ions, and positive, negative and neutral MSPs. Reprinted from Baumann et al. [2013]

3

MAXIDUSTY-2 Rocket Campaign

This chapter will discuss the planned MXD2 rocket campaign and the payload instruments onboard. We start with a general outline of the mission concept and its motivation, continuing with an overview of the different payload instruments, and their objectives. We end with a more in depth description of the MESS instruments current design and experimental expectations.

3.1 Mission concept

In-situ observations are a vital part of understanding the process governing MSPs in the Earth's atmosphere. Ground based instruments like incoherent scatter radars can measure MSP properties such as number densities and radii [Strelnikova et al., 2007, Rapp et al., 2007]. In-situ measurements prove more feasible for retrieving information like charge number [Havnes et al., 1996, Rapp et al., 2010, Antonsen and Havnes, 2015, Plane et al., 2014] and in theory the composition of MSPs [Hedin et al., 2014]. Recently Hervig et al. [2021] published a method for retrieving MSP composition estimates through satellite observations through the Solar Occulation For Ice Experiment (SOFIE) instrument mounted on the Aeronomy of Ice in the Mesosphere (AIM) satellite. The research showed that the composition of smoke particles in the meso-

sphere coincides well with iron-rich olivine ($Mg_{0.8}Fe_{1.2}SiO_4$). Laboratory experiments [Saunders and Plane, 2006, 2011] support this conclusion, providing a possible foundation for MSP composition. An analysis of directly sampled MSP material could further help develop our understanding of the true composition of MSPs.

The MXD2 rocket is expected to launch from Andøya Space, Oksebåsen, Norway in either June, July or August and preferably during observed PMSE/NLC. The aim of the campaign is to study charged mesospheric dust/smoke particles, ice particles and plasma conditions in the MLT region, as well as retrival of MSP samples from two independent instruments. MXD2 is part of the Grand Challenge Initiative project mesosphere/lower thermosphere; a project aimed at studying the mesosphere/lower thermosphere region with both airborne and ground-based instruments. The Grand Challenge Initiative is a collaboration between several international research institutes, developed by Andøya Space, University of Oslo (UiO) and National Aeronautics and Space Administration (NASA).

The MXD2 payload will consist of eight different in-situ instruments, two of which are MSP collection instruments. The rocket observations will simultaneously be supported by ground based optical and radar instruments, measuring the ionospheric plasma conditions and PMSE/NLC activity. Further, we will give a short summary of all instruments mounted on MXD2 rocket, with an extended focus on the MESS instrument. We use the notation dust and smoke particle interchangeably.

3.1.1 DUSTY

First flown in 1994, the in-situ DUSTY probe was the first to detect charged dust particles in the mesosphere [Havnes et al., 1996, Antonsen and Havnes, 2015]. DUSTY is a Faraday cup dust detector developed by UiT. The three main parts of the instrument are two oppositely charged grids G1 and G2, and a dust collection plate DC (Figure 3.1). Dust particles will enter through the opening at the top of the instrument. The first grid G1 is positively charged, while the second grid G2 is negatively charged, and is mounted just below G1.

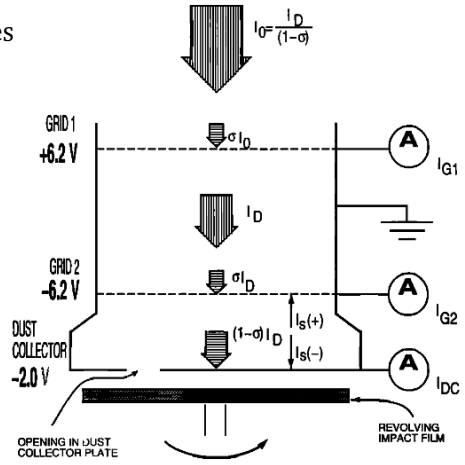

Figure 3.1: Schematic illustration of DUSTY [Havnes et al., 1996]

G1 and G2 is designed to shield
against ambient ions and electrons. The DC plate is located below the G2 grid, with a small opening to potentially allow for dust particles to stick to the rotating impact film just below. Only dust particles should impact G2 and the DC due to the shielding from G1 and G2. The charged dust will produce a current upon impact due to the carried charges or heavy impact secondary plasma production [Havnes and Næsheim, 2007]. From these measurements the number density of charged dust particles along the rocket trajectory can be estimated. Due to the aerodynamic properties of the probe it is assumed that 2 nm dust particles and larger will enter the probe.

3.1.2 MUDD

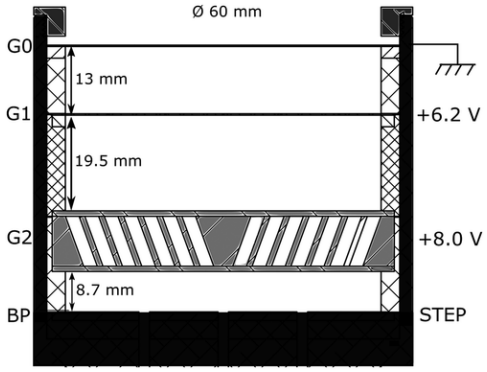

Figure 3.2: Schematic illustration of MUDD [Antonsen et al., 2017]

MUltiple Dust Detector (MUDD) is a modified version of DUSTY, also developed at UiT [Antonsen et al., 2017]. MUDD consist of three grids(G0, G1 and G2) and a bottom plate (BP) (Figure 3.2). G0 is biased to the payload ground, and shields other instruments from MUDDs' internal electric field. G1 is similar to DUSTY, with the same purpose of shielding out ambient plasma. G2 however, consist of partly overlapping inclined rings, such that dust particles on perpendicular trajectories into the probe will not pass thought the grid, and instead collide and generate a measurable charge. The BP is biased in different voltage steps throughout the flight and acts in a similar way to the DC on DUSTY. A varying biased potential will provide a size distribution of the colliding dust particles. Two MUDD probes are intended to fly on MXD2. Two probes set to different operational modes on the BP will increase the resolution and accuracy of the measurements.

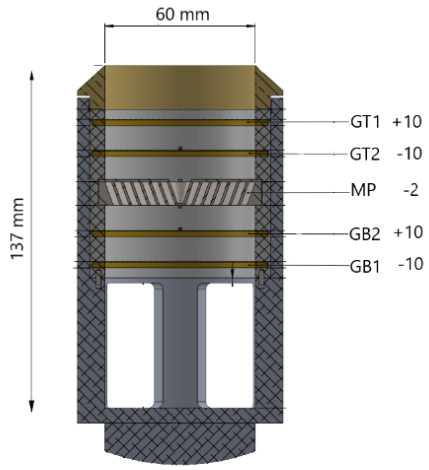

Figure 3.3: Schematic render of SPID [Trollvik et al., 2019]

3.1.3 SPID

The Smoke Particle Impact Detecter (SPID) [Gunnarsdottir, 2019] is again a modification of the Faraday cup designed at UiT, with both MUDD and DUSTY as forerunners. Compared to MUDD, SPID has an open-end design, allowing the airflow to pass completely through the instrument and thus reducing the shock front (Figure 3.3). This will also reduce the internal air pressure of the instrument, allowing for smaller particles to be detected. The inclined ring grid (middle plate, MP) is designed to measure impacting smoke particles, in addition to fragment ice embedded MSPs. The MP has a bias potential relative to the payload floating potential. Two wire grids both positively and negatively charged, situated both above (GT1, GT2) and below (GB1, GB2) the MP are designed to shield out the ambient plasma. The open end design requires the two biased wire grids below the MP to assure plasma shielding from the bottom. SPID was flown on the student rocket G-chaser through the RockSat-XN program and Grand Challenge Initiative in 2019 [Trollvik et al., 2019].

3.1.4 CONE

COmbined sensor for Neutrals and Electrons (CONE) is designed and operated by the Leibniz - Institute of Atmospheric Physics at Rostock University in Kuehlungsborn (IAP). CONE is an instrument for mainly measuring neutral air density with a high spatial resolution. See Strelnikov et al. [2013] and references within for a detailed description of CONE.

3.1.5 m-NLP and Faraday rotation experiment

A multi-Needle Langmuir Probe (m-NLP) from UiO will measure the absolute electron density with high enough resolution to observe small scale plasma structures [Jacobsen et al., 2010]. Comparing small-scale structures in the electron density to dust densities will provide information on the dust influence on the charge balance of the MLT region. Additionally, a Faraday rotation experiment from IAP allows for electron density measurements independent of payload charging and aerodynamics [Friedrich et al., 2013]. As a linearly polarised electromagnetic wave travels through a magnetic field with a component in the waves' propagation direction, the polarisation plane of the wave rotates. The angle of rotation is then used to find the electron density with respect to altitude between the ground station and rocket.

3.1.6 MAGIC

One of the two in-situ sample collection instruments to be flown on the MXD2 rocket is the Mesospheric Aerosol - Genesis, Interaction and Composition (MAGIC) instrument. MAGIC has been flown on multiple sounding rockets between 2005 and 2011, both during summer and winter conditions [Hedin et al., 2014]. Up to nine pins are placed in a circulatory revolver–like mechanism, which extends individual sampling pins at certain altitude intervals. One or two pins are not extended, and are used as a reference sampling surface to determine potential contamination during preparation and transport. The pins are designed such that they can be extended outside the payloads shock front to reduce the aerodynamic filtering from the air flow. Each pin is equipped with a 3mm wide transmission electron microscopy (TEM) grid as the sampling surface. The MSPs are expected to directly stick onto the sampling surface.

In practise, it is highly uncertain how the true sticking efficiency for the MSPs and the shock front filtering influence the results (J. Hedin, Personal communication, February 22, 2023). At the time of writing, the MAGIC instruments have not managed to produce concrete evidence of MSPs in the mesosphere. Multiple experiments have been subject to heavy contamination of the sampling surfaces both pre- and post-flight. The last MAGIC flight, during the Particles, Hydrogen and Oxygen Chemistry in the Upper Summer mesosphere (PHOCUS) project, only one pin was exposed during the flight and all other pins were used as references prepared in different ways. This was done to reduce the possibility of contamination to an absolute minimum. No new particles was found on either the reference pins nor sample pin. This shows how much of a challenge collecting and returning MSPs from the mesosphere appear to be. With the knowledge gained through previous in-situ sampling missions, new methods and concepts can be developed to improve the results.

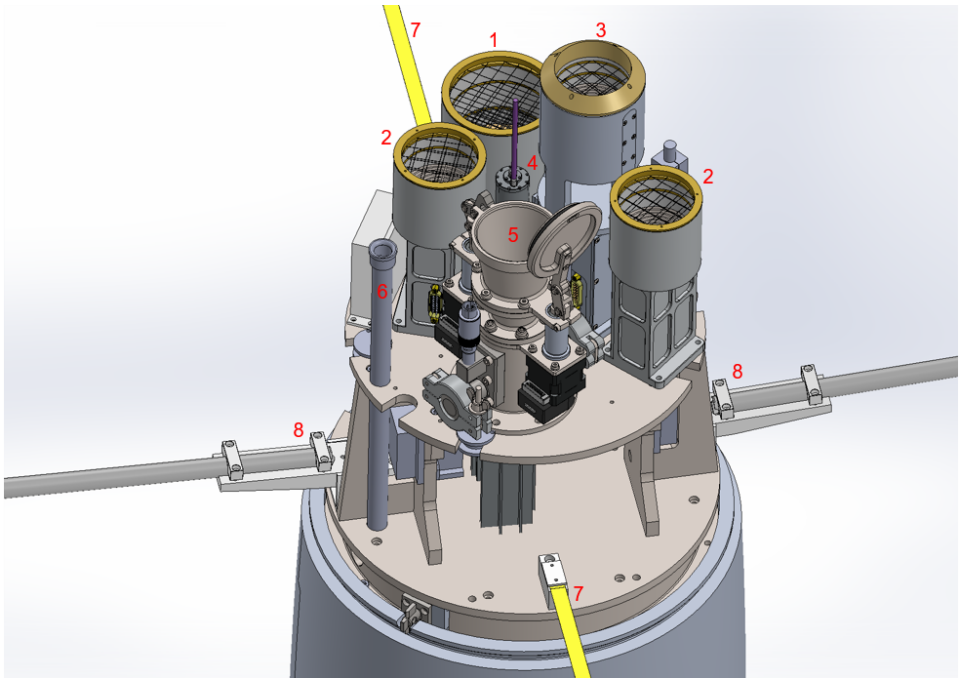

Figure 3.4: Current configuration of the MXD2 payload consisting of DUSTY (1), MUDD (2), SPID(3), MAGIC (4), MESS(5), CONE (6), Faraday rotation experiment (7), m-NLP(8). Reprinted from Mann et al. [2022].

3.2 MESS

The results from the PHOCUS campaign highlight the uncertainties regarding sticking efficiency of MSPs onto the collection surface and aerodynamic filtering. MESS [Havnes et al., 2015] was designed with the goal of reducing the aerodynamic filtering effect. It is designed to collect both mesospheric ice particles and pure MSPs. It is suggested that mesospheric ice particles consists of around 0.01% to 3% MSP [Hervig et al., 2012]. Ice particles, much heavier than MSP are expected to be less influenced by the aerodynamic flows from the payload due to their larger momentum. By sampling ice particles in combination with pure MSPs, it is expected to increase the probability of sampling MSPs during flight.

MESS (Figure 3.5) consist of a cone-shaped funnel angled at 75° with a sampling area (top of funnel) of 19.635 cm^2 and a collection area (bottom of funnel) of 2.545 cm^2. A covering lid completely shields the sampling surface during launch and descent of the payload. Two stepper motors control the lid movement. One motor controlling the opening/closing of the lid itself, and the other one controls a locking hinge to secure the lid while in closed position.

A persistent mesospheric ice particle layer like NLC/PMSE layers is required for the MESS instrument to operate as expected. The sampling surface

is first exposed somewhere close to the lower boundary of the ice particle layer, and closed before exiting the upper boundary. The walls of the funnel are designed such that colliding particles can be deflected towards the collection area. Thus, the sampling area is increased while keeping the collection area comparatively small. Similar to the MAGIC instrument, a TEM grid is used as the sampling surface. This enables the MSPs to be sampled directly onto an analysable surface, reducing the likelihood of contamination post flight. Two TEM grids are mounted vertically, whereas the lower one is never exposed and used as a reference grid to identify potential contamination.

The sampling surface is shown at the bottom of the funnel in Figure 3.5, with the reference surface just below, completely seperated from the exposed chamber. Figure 3.5 shows the instrument configured for laboratory tests with two elongated pressure sensors on each side of the instrument and an open pressure valve. Figure 3.6 shows the instrument in operational mode with the pressure sensors removed and the pressure valve closed.

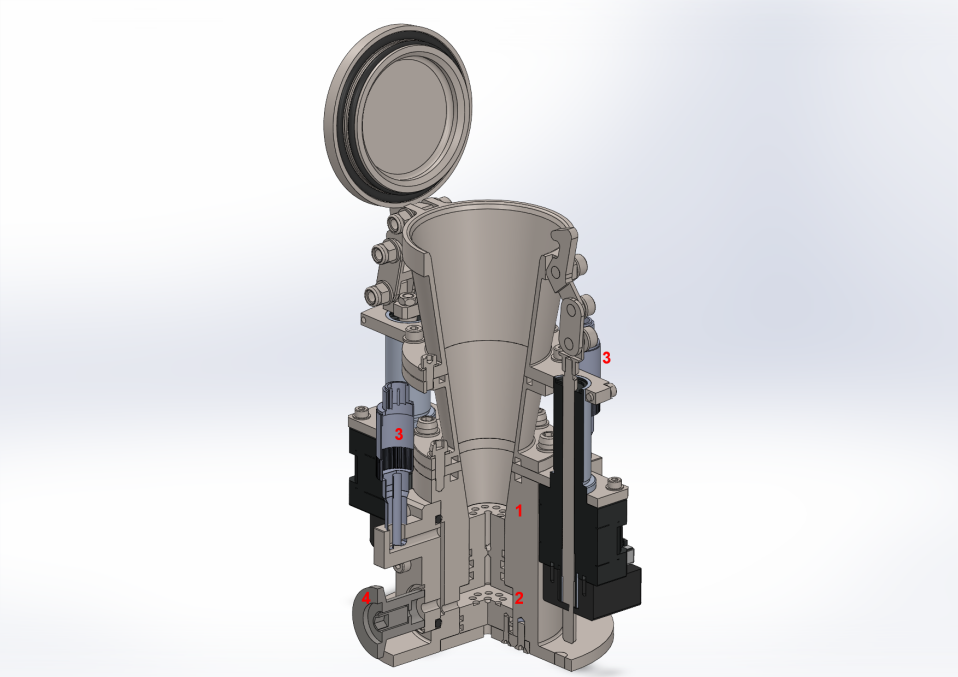

Figure 3.5: A sliced view of MESS, showing the funnel shape and the sampling surface (1) and reference surface (2). (3) indicate two pressure sensors, and (4) shows the open pressure valve. Figure provided by Sveinung V. Olsen.

Pineau et al. [2023] simulated the particle trajectories and resulting detection efficiency for inbound particles. The incoming particles are seperated into two cases; primary and secondary particles. Primary particles are directly impacting the sampling surface i.e., the incident angle is parallel to the normal of the sampling surface. Secondary particles have collided with the funnel walls

and fragmented before impacting the sampling surface. The ice component of the particles are then assumed to be evaporated due to fragmentation. The simulated sizes for pure MSPs have a radius between 1 and 10 nm, and a radius between 10 and 50 nm for ice particles.

In the case of primary particles the collection efficiency depends on the neutral air distribution inside the instrument. For a rocket velocity of 800 $m.s^{-1}$, the simulation yielded a cut–off at 85km for particles with radii 5 nm, and 80 km for 10–15 nm particles. In the case of the secondary particles the simulations yielded a collection efficiency of 0.8, in relation to the amount of particles entering the instrument. As stated by the authors, this number is highly uncertain due to the complexity of the particle funnel-surface interaction. They conclude with that MESS will be able to collect a significantly higher amount of particles at 85 km altitude than at 80 km.

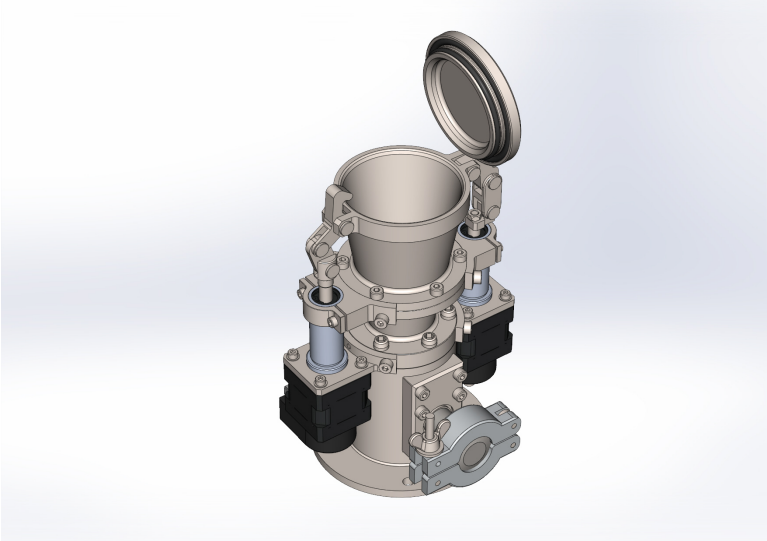

Figure 3.6: Current design of MESS in the open configuration. Figure provided by Sveinung V. Olsen.

4

Method

The aim of this chapter is to explain the methods and decisions that led to the results presented in this thesis. First we introduce the simulation WACCM/-CARMA, which was used to produce the data and results presented in chapter 5. In the same section we present the model data outputs and following assumptions. In section 4.2 we present the unit transformations applied to the model data, specifically MSP concentration and altitude data. Section 4.3 describes the selection of months and the analysis of MSP variations. Lastly, we show how the MSP collection estimates are derived, and the assumptions we make. The collection efficiencies for MESS is shown in table 4.2 and 4.3, which were acquired from Pineau et al. [2023].

4.1 WACCM/CARMA model description

The data discussed in this thesis are a result of a coupled simulation run of the Whole Atmosphere Community Climate Model 4 (WACCM) [Richter et al., 2008] and the Community Aerosol and Radiation Model (CARMA) [Turco et al., 1979, Toon et al., 1979] called the WACCM/CARMA model. The dataset used is the same as discussed in Gunnarsdottir et al. [2023] in regards to their MSP density profiles. WACCM/CARMA was produced by the University of Leeds and the dataset was generated on October 30^{th} 2019, and provided by Dr Wuhu Feng.

WACCM is a global circulation climate model that models the wind pat-

terns and transportation systems in Earth's atmosphere. The simulation uses Community Earth System Model version 1.0 (CESM1.0) as its numerical framework. WACCM considers the troposphere-mesosphere coupling and the circulation patterns of the atmospheric constituents through atmospheric temperatures, and zonal and vertical winds. CARMA is a multidimensional microphysics model tracking and simulating the physics of meteoric particles and gases together with a dynamical model, in our case WACCM. CARMA calculates the evolution of the constituents based on inputs from WACCM. The CARMA results are passed back into WACCM as constituents, modifying the model's parameters before the next iteration.

The horizontal resolution of the model is $1.9° \times 2.5°$ (latitude $\times$ longitude) with 96 and 144 increments respectively. The vertical resolution is 66 pressure levels between ground level and ~145 km, with steps of ~3.5 km in the MLT region. The simulation covered a 22-year period, with monthly averaged data outputs.

Initial particle sizes are 0.2 nm, with an assumed material density of 2 g/cm^3 [Saunders and Plane, 2011]. Further coagulation and sedimentation will occur throughout the MSPs' path through the atmosphere. The coagulation coefficients include convective, Brownian and gravitational effects, while the sticking efficiency is fixed at 100%. The output parameters of the model simulation are the distribution of MSPs throughout the atmosphere, along with atmospheric temperature, pressure, and spatial coordinates. It provides both individual particle size distributions and a combined total number density. The MSP concentration data is structured into 28 bins of radii from 0.2 nm to 102.4 nm. Table 4.1 shows all the available output parameters. For further details on WACCM/CARMA we reference Bardeen et al. [2008] for the first three-dimensional simulation of meteoric dust in a general circulation model.

The initial MSPs are generated through a globally uniform source function. The meteoric source function used in this simulation run is uncertain. According to personal communication with Dr Wuhu Feng the model parameters are as described by Brooke et al. [2017], where the meteoric source function is around 7.9 $t.d^{-1}$ or 2.8 $kt.y^{-1}$. At the time of writing we contacted the model provider for further information. Bardeen et al. [2008] present results from 6 simulations with varying conditions and meteoric source functions of about 16 $kt.yr^{-1}$ and 32 $kt.yr^{-1}$. Figure 4.1 shows the July zonal average number density and mass density of MSP larger than 1 nm from simulation 4. The WACCM/-CARMA version used in this thesis are of a newer version than the one used by Bardeen et al. [2008]. In section 5.2.1 we will present a comparison between our results and Bardeen et al. [2008].

Table 4.1: Output parameters from the WACCM/CARMA model simulation. Cumulative over all size bins indicates that the parameter can be regarded as a total, and are not available for each individual size bin.

Parameter (unit)	**Notes**
Dust mass mixing ratio (kg/kg)	28 size bins (0.20–102.4 nm)
Dust surface area density (cm^2/cm^3)	Cumulative over all size bins
Dust mass density (g/cm^3)	Cumulative over all size bins
Dust number densit ($\#/cm^3$)	Cumulative over all size bins
Latitude ($^\circ N$)	96 steps
Longitude ($^\circ E$)	144 steps
Hybrid sigma level pressure (level)	66 steps
Surface Pressure (Pa)	
Temperature (K)	
Geopotential height (m)	Above sea level

Figure 4.2 shows the total January MSP number density above 69.9°N 19.2°E for all 22 model years. We see that the model appear to reach a steady state in the middle and upper atmosphere first, just after year 1. The lower atmosphere/troposphere seem to reach steady state after the second year. The first year only includes data for January, February and March. Due to the incomplete dataset and non-steady state for the first year we exclude this year from the analysis. Even though our analysis is focused on the mesosphere, conservatively we choose to exclude the second year from the analysis as well.

4.2 Unit transformations

As common in metrological model simulations, WACCM/CARMA provides either sigma pressure coordinates or geopotential height as vertical coordinates. For further information on sigma pressure and geopotential height, see Holton [2004]. The small variations in pressure in the upper atmosphere makes pressure coordinates impractical for representative purposes, thus we choose to represent altitude in meters. Geopotential height is defined in SI units as the work done by raising a parcel of one kilogram one meter under standard gravity. An approximation to the geopotential height Φ is given by Equation 4.1, where z is the height above mean sea level.

$$\Phi(z) = \frac{gR_e z}{R_e + z} \tag{4.1}$$

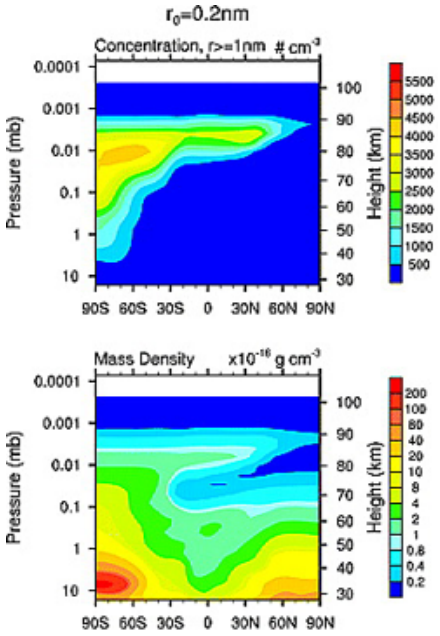

Figure 4.1: Number density and mass density results for MSP bigger than 1 nm from simulation 4 by Bardeen et al. [2008]. The initial MSP size is 0.2 nm with a source function of 16 kt yr^{-1}. Reprinted from Bardeen et al. [2008]

Whereas R_e is the average Earth radius, and g is the gravitational acceleration, given by Equation 4.2, with g_0 as the standard gravity.

$$g(z) = g_0 \left(\frac{R_e}{R_e + z} \right)^2 \tag{4.2}$$

The gravitational variations in the latitudinal direction due to centrifugal effects is not accounted for, only the vertical variation is considered.

One of the most common ways of representing a mixing ratio in atmospheric models are through mass mixing ratio [kg/kg]. However, the most common way of representing MSP densities in upper atmosphere literature is through number densities [#/cm^2]. A conversion from mass mixing ratio for MSP n_r to number densities N_r are achieved through Equation 4.3 by multiplying the mass mixing ratio with the density of air, found through the ideal gas law (Equation 4.4), and dividing by the mass of one particle (Eq. 4.2). The individual MSP size intervals are further denoted N_r, and the total number density N_D, both with unit #/cm^2.

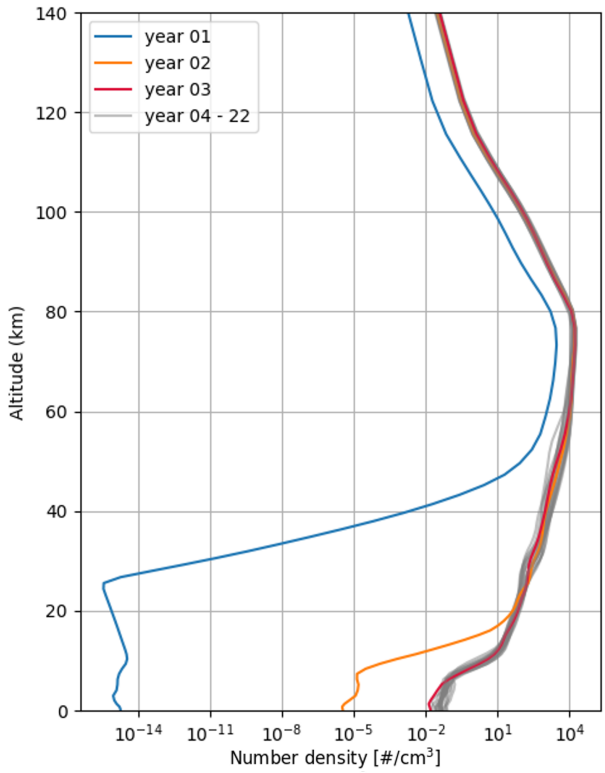

Figure 4.2: Total number density in January for model years 1 to 22, with years 1, 2 and 3 highlighted in blue, orange and red respectively. Years 4 to 22 are displayed in a diffuse gray color. The model grid point is 69.9°N 19.2°E.

$$N_r = \frac{n_r \rho_A(p,T)}{m_p(r)} \tag{4.3}$$

where the air density $\rho_A(p,T)$ at a given pressure level $p\,[Pa]$ and temperature $T\,[K]$ is

$$\rho_A(p,T) = \frac{p}{R_s T}\,. \tag{4.4}$$

The mass of one spherical particle with radius $r\,[m]$ and density $\rho_P = 2000\ [\mathrm{kg/m^3}]$ is

$$m_p(r) = \frac{4\pi}{3} r^3 \rho_p \ .$$

For the air density we have assumed dry air with a gas constant of $R_s = 287.05$ [J/kg K]. To validate the approximation we compare the total particle number density provided straight from the model output, denoted N_D, with the sum of the individual number densities for each particle size, denoted ΣN_r, shown in Figure 4.3. In the right panel we see that the maximum difference in the yearly mean between N_D and ΣN_r is around 200 $/cm^3$ or a 2.5% difference.

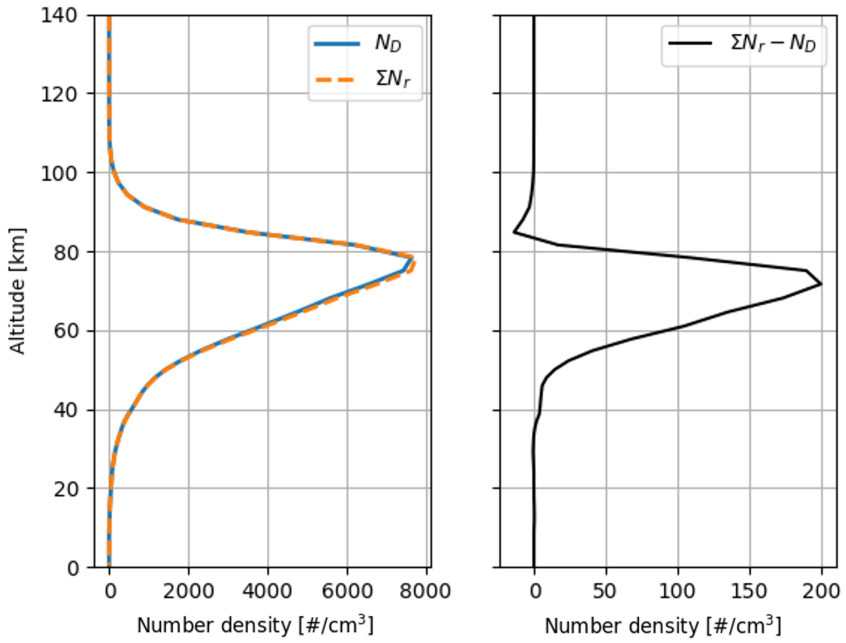

Figure 4.3: Yearly mean of the total MSP number density from the WACCM/CARMA model N_D, shown together with the approximation to the total MSP number densities as a sum of each MSP size intervals ΣN_r (left), and the difference between them (right). Note the different scales on the horizontal axis.

4.3 MSP variations analysis

As MXD2 will launch from Andøya Space, Oksebåsen, Norway (69.3°N 16°E), we want our analysis to focus on this area. The model has a horizontal resolution of 1.9° × 2.5° (latitude × longitude) and the closest model grid point

is 69.9°N 19.2°E. Thus, all the data presented in our analysis are results from this data point.

The exact altitudes in which MESS will perform its sampling process are not yet determined. Pineau et al. [2023] have simulated the particle trajectories for MSP and ice particles within MESS at different altitudes between 80 and 90 km. The simulated initial MSP sizes were from 1 to 10 nm. However, it is expected that larger particles will reach the collection area regardless. We have therefor chosen to focus our analysis on the same region and similar particles sizes.

In our analysis of the MSPs monthly and yearly variations we primarily focus on the months June, July and August, as these are the candidate months for the MXD2 campaign. We present results from MSP size bins with the radii of 1.008, 2.016, 3.2, 4.032, 6.4 and 8.0623 nm. The model output provides a finer resolution of MSP sizes than shown here, but we have chosen these sizes for representative purposes. We show the variation in MSP concentration both throughout the whole air column from 20 to 100km, and a more focused view from 80 to 90 km. We show the winter months as dotted lines such that the summer months are the main focus. In the 80 to 90 km view, the months June, July and August are marked such that they are easier to distinguish.

In the year-to-year analysis we show the combined number density of MSPs between 1 and 10 nm, only for June, July and August. We show all years from year 3 to 22. At stratospheric altitudes, large MSPs dominate the total concentration, while in the mesospheric region these particles appear to be negligible. Thus, as to focus on the variations in the mesosphere we again exclude larger particles than 10 nm. We also show the average of the total number density over the twenty-year period to make the variations more clear.

4.4 MSP collection with MESS

In this section we attempt to estimate the amount of particles that can be collected by MESS between 80 and 90 km. First we calculate the cumulative amount of particles potentially collected if the collection efficiency of MESS is 100%. We then combine these results with the collection efficiencies of MESS from Tables 4.2 and 4.3. The collection efficiency is the ratio between the number of particles entering the funnel and number of particles that reach the collection area. The potential external aerodynamics effects are not accounted for, only the internal. A lower rocket speed results in a higher collection efficiency, while a higher rocket speed results in a lower efficiency. The previous MAXIDUSTY rocket, MXD1, had a speed of around 800 $m.s^{-1}$ at an altitude of 80 km. At the time of writing, the exact rocket engine which will be used on the MXD2 rocket is not decided and thus the speed of the rocket is uncertain. It is speculated that the proposed rocket engine may result in higher speeds

compared to MXD1. We then have chosen to analyse rocket speeds of 800 and 1000 m.s^{-1}. A lower rocket speed would result in a slightly higher collection efficiency for all MSP sizes.

The funnel entrance on MESS has an area of $A_f = 19.635$ cm^2 and a collection area situated at the bottom of the funnel of $A_c = 2.545$ cm^2. This equals a ratio of $\frac{A_f}{A_c} = 7.715$ between the funnel entrance and collection area. We assume the funnel to be fully exposed at 80 km and that during the opening (and closing) of the lid no particles are collected.

The WACCM/CARMA model has a vertical resolution that changes with altitude, and the approximate altitudes used by the model between 80 and 90 km are 79.8, 81.9, 83.4, 86.1, 88.5 and 91.0 km. Equation 4.5 shows the amount of collected particles N_c^r with size r over the distance h_0 to h, with a collection efficiency C_e and MSP number density N_r.

$$N_c^r(h) = \frac{A_f}{A_c} \int_{h_0}^{h} N_r(h')\, C_e(h')\, dh' \tag{4.5}$$

Here h_0 denotes the initial altitude, and h the final altitude. In this case, $h - h_0$ would be the distance between the altitude increments from the model output. We also present an estimate of the total amount of particles collected as a sum of all collected particles at each altitude. Particle sizes in which the estimated amount of collected particles at 90 km is less than one are not included in this analysis, and we consider these as undetectable by MESS.

Lastly, we consider the case if MESS was to end its sampling process at 95 km instead of 90 km, to investigate the effects of expanding the sampling distance. In the case of a rocket speed of 1000 m.s^{-1} and MSP size 1 nm, the difference in collection efficiency from 85 to 90 km is 45%, and 70% for the 2 nm MSPs (table 4.3). If we assume that the collection efficiency follow a similar trend, the collection efficiency at 95 km for all MSP sizes can be assumed to be close to 100%. Again we exclude MSP sizes that show less than one MSP /cm^2 on the collection surface at 95 km. We assume similar trends for a rocket speed of 800 m.s^{-1}. Note that this is a rough estimate, and only based on speculations from the authors.

Table 4.2: Collection efficiencies for MESS with a rocket speed 800 $m.s^{-1}$ between 80 and 90 km as found by Pineau et al. [2023].

	Altitude			
Radius	80 km	82 km	85 km	90 km
1 nm	0%	0%	0%	50%
2 nm	0%	0%	0%	75%
3 nm	0%	0%	46%	84%
4 nm	0%	0%	59%	93%
5 nm	0%	44%	70%	100%
6 nm	0%	50%	75%	100%
7 nm	43%	55%	79%	100%
8 nm	48%	62%	83%	100%
9 nm	50%	68%	85%	100%
10 nm	55%	72%	82%	100%

Table 4.3: Collection efficiencies for MESS with a rocket speed 1000 $m.s^{-1}$ between 80 and 90 km as found by Pineau et al. [2023].

	Altitude			
Radius	80 km	82 km	85 km	90 km
1 nm	0%	0%	0%	45%
2 nm	0%	0%	0%	70%
3 nm	0%	0%	34%	80%
4 nm	0%	0%	50%	86%
5 nm	0%	0%	59%	95%
6 nm	0%	45%	68%	100%
7 nm	0%	50%	76%	100%
8 nm	37%	54%	78%	100%
9 nm	45%	58%	80%	100%
10 nm	50%	63%	82%	100%

5

Results and Discussion

In this chapter we present the results from our analysis of MSP conditions in the mesosphere based on data from the WACCM/CARMA model. Additionally, we provide an estimate for the amount of MSPs that can be expected to be collected by the MESS instrument under certain conditions. We discuss the presented results from the perspective of the MXD2 rocket campaign and how these results can contribute to the planning of the campaign. The results and discussion are seperated into three sections; yearly and monthly variability of MSP, and the estimates for the collection of MSP with MESS.

5.1 Monthly variation in MSPs

As the atmospheric wind circulation globally transport meteoric particles, the particle density throughout the whole air column changes with each month. In the mesospheric winter polar region, a downward flux of air compresses the mesosphere. The downward circulating air drags suspended particles along with it, down to lower altitudes. Oppositely, in the polar summer mesosphere, an upwards flux of air pushes the particles to higher altitudes. This global circulation pattern can be shown through the WACCM/CARMA model simulation. As the particle collection mechanism of the MESS instrument have been simulated for particles from 1 to 10 nm, we present the vertical particle distribution for similar sizes.

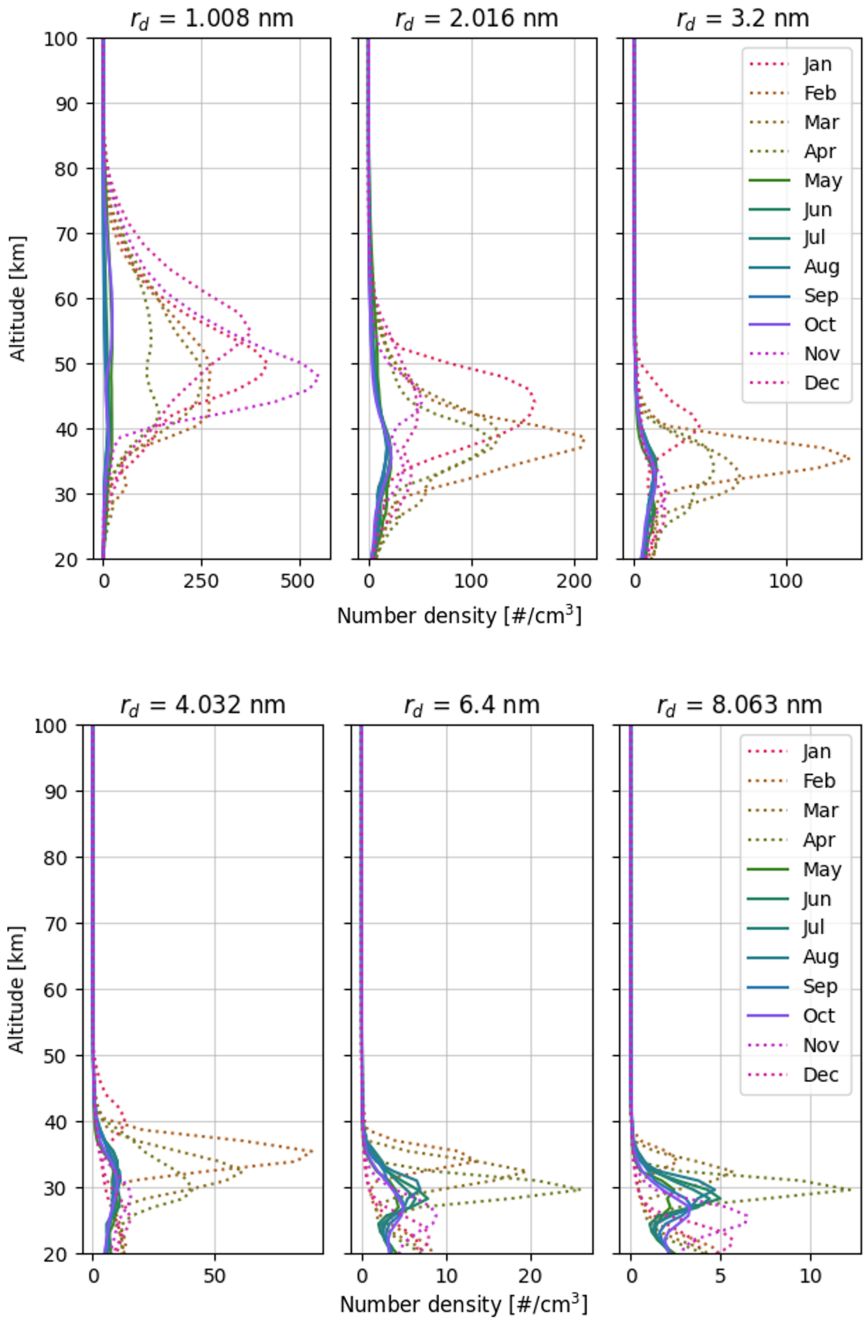

Figure 5.1: Monthly averaged MSP density throughout the last model year for particle radius from 1.008 to 8.063 nm. Winter months are shown as dotted lines. Note the different scales on the horizontal axis.

In Figure 5.1 we show the vertical particle density for sizes from 1.008 to

8.062 nm. For particles with radius 1.008 nm, the maximum concentration is between 40 and 50 km in November. This is also the highest concentration of particles of sizes between 1 and 10 nm throughout the whole year. For both radius 2.016 and 3.2 nm the altitude of maximum concentration are below 40 km. We also see that the month of maximum concentration is now February as opposed to November for the 1 nm particles. For 3.2 nm particles we see that the January concentration has decreased significantly compared to the 2.026 nm particles. As the particle size increase from 1 nm, we also see that the January peak concentrations are situated at higher altitudes than other months. It appears that the most abrupt fluctuations in particle concentration is found during the winter months. During summer, the monthly fluctuations appear significantly lower and more stable. In addition, we note that the width of the vertical distributions decrease with increasing particle sizes.

In case of the 4.032 nm particles we see similar profiles to that of the 3.2 nm particles, with February being the month of the highest concentration and rapidly decreasing towards the summer months. For sizes 6.4 and 8.063 nm the month of the highest concentration has now changed to April. A 40 km January peak is still present for 4.032 nm particles, but disappears for larger sizes. The profiles follow the trend mentioned, where generally all particles sink to lower altitudes as the sizes increase.

A closer inspection of the profiles between 80 and 90 km (Figure 5.2) shows a higher concentration of particles bigger than 1 nm during the summer months compared to the winter months. This is opposite to the trend we see at lower altitudes, where usually the highest concentration is found during the winter months. Again we see that the bigger particles are, the lower their densities appear to be. We have marked the months June, July and August as these are the candidate months for the launch of the MXD2 rocket. For the 1.008 nm particles, the particle densities during June, July and August are between 0.01 and 1 $/cm^3$. As the particle sizes increase from 1.008 nm, July, June and August seem to dominate as the months of the highest particle densities. The densities rapidly decrease towards 10^{-5} $/cm^3$ and less as the altitude increase. For the 8.063 nm particle size at the altitude between 80 and 87 km we see a number density between 10^{-3} and 10^{-5} $/cm^3$ for the months June, July, August and September.

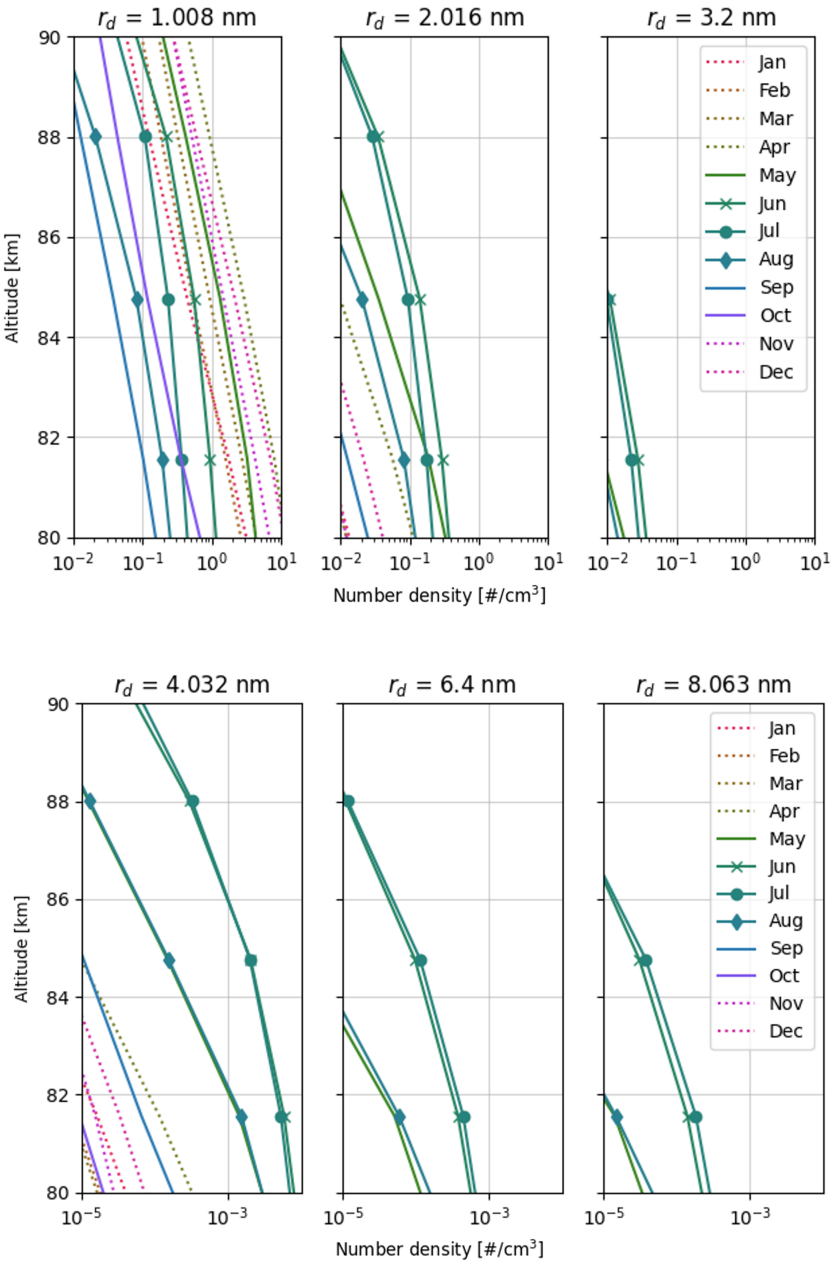

Figure 5.2: Monthly averaged MSP density between 80 and 90km for particle radius from 1.008 to 8.063 nm. The potential months for the MXD2 rocket campaign is marked. Note the different horizontal scales. The three top and three bottom figures share horizontal axis such that the variation between sizes are clearer.

5.1.1 Discussion

As previously stated, the months June, July and August have been picked as the main candidates for the launch of the MXD2 campaign, due to the potential NLC and PMSE layers during this time period. From Figure 5.1 it is clear that the winter months generally exhibit higher densities than the summer months, especially at stratospheric altitudes.

In the altitude region 80–90 km, shown in Figure 5.2, we see that the purposed campaign months June, July and August appears to have the highest densities for most of the particles sizes. Generally it appears that June or July has the highest density of particles in the 80–90 km region. This is somewhat unexpected as the meridional circulation is generally expected to transport mesospheric constituents away from the summer pole. A possible explanation could be that as the MSP is transported to the winter pole, the downward forcing from the meridional circulation together with gravitational forcing pushes the MSP to lower latitudes. At the summer pole the process would be reversed, whereas the two forcing mechanism works in opposite directions, causing bigger MSP to be suspended in the summer mesopause region. In Figure 5.1 it is apparent that during winter months (dotted lines) the majority of MSP is situated below 70 km, and below 40 km for particles bigger than 4 nm. During the summer months, the MSP densities appear more distributed throughout the atmosphere. In the case of the 8 nm particle size bin, it appears that most of the densities is concentrated below 40 km throughout the whole year. This could indicate that the larger MSP sizes are more influenced by the gravitational forcing rather than the forcing due to the atmospheric circulations. The results presented here support the idea that June, July or August are viable campaign months.

Compared to lower altitudes, the 80–90 km region show very low values of particle densities, mostly less than zero particles $/\mathrm{cm}^3$. Due to the low density of particles a large sampling area is needed to achieve preferable results (see section 5.3).

5.2 Year-to-year variation in MSPs

It is important to not only consider the monthly variations, but also the potential year-to-year fluctuations. A twenty-year model simulation could give us an indication to how much the particle number density during certain months fluctuate, and if this is important to consider when planning the date for the rocket flight.

In Figure 5.3 we show the averaged particle number density for June, July and August throughout the last twenty years of the model run. The average

value for each month is shown as a dashed red line. The MSP density in June appears to fluctuate more than July and August at altitudes below 60 km. The biggest variation is seen in July at 50 km, varying from a minimum particle density of 50 /cm^3 to a maximum of 100 /cm^3.

In Figure 5.4 we limit the vertical range to between 80 and 90 km and use a logarithmic scale on the horizontal axis. Here, the particle density vary between 0.9 and 5 /cm^3 depending on the month, with June having the overall highest densities.

Figure 5.5 presents similar results as Figure 5.4, however presented in mass density rather than number densities. We assumed the MSP to be spherical particles, with a material density of 2 g/cm^3. Figure 5.5 is shown in an attempt to compare with previous model simulations of WACCM/CARMA. This will be discussed in the following section.

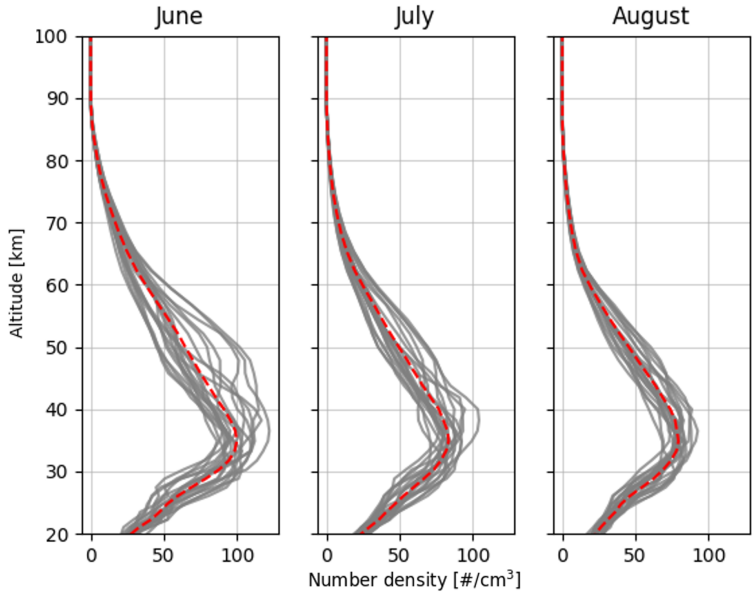

Figure 5.3: Total particle concentration for sizes from 1.008 to 8.063 nm over the last twenty model years (year 3 to 22). The Red dashed line shows the average particle concentration over the twenty years. Gray lines shows the individual yearly profiles.

5.2.1 Discussion

Yearly stability is important to consider when deciding when to perform the rocket campaign. For consistency throughout previous and future studies, one would often like to analyse as similar and stable conditions as possible. The yearly variability in each month is then an important factor to consider. Look-

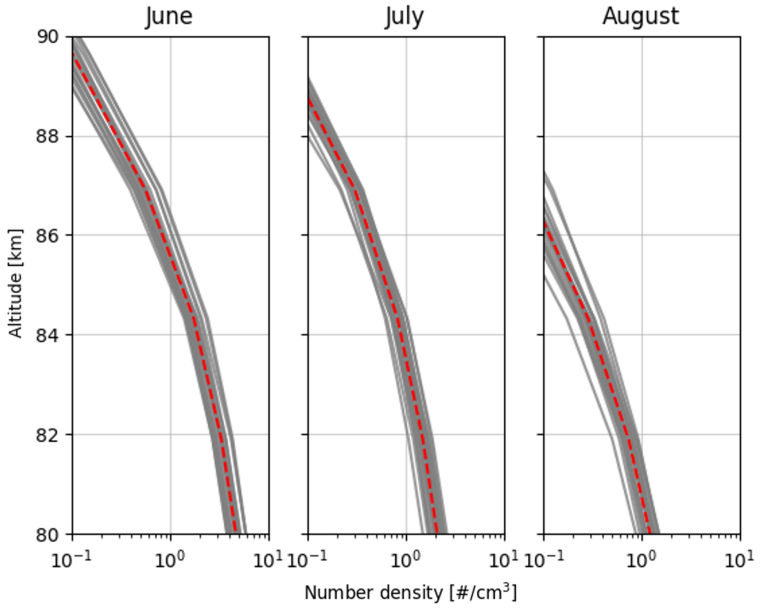

Figure 5.4: Similar to Figure 5.3 but limited to altitudes from 80 to 90 km and a logarithmic horizontal axis.

ing at the whole 20–100 km air column (Figure 5.3), June appear to vary the most out of the candidate months for the MXD2 campaign, and August the least. However, these variations are most apparent at altitudes not important for the MSP collection experiments.

From Figure 5.4 there appears to be very little yearly variation at altitudes 80–90 km. Such small variations from year-to-year gives good premises for conducting experiments. Based on these model results it can appear we can neglect the yearly variation in MSP densities at altitudes between 80 and 90 km. Additionally, the results suggest that the choice between July, June or August has little impact on the experiment results. However, June does appear to have the highest number density out of the three months, which could be of importance if the amount of particles is a limiting factor in an experiment. In case of previous MAGIC flights, the lack of successfully collected particles during previous MSP collection attempts with rockets, are mainly speculated to be because of the aerodynamic effects and sticking efficiency of MSP to the collection surface (see section 3.1.6). If the aerodynamic effects plays a bigger role than previously thought, similar experiments could potentially benefit from a higher particle density to increase the chance of penetrating particles. The premises of the funnel design on MESS is to increase the sampling area in an attempt to collect more particles, while keeping the collection area small. The MESS instrument would then benefit from the apparent higher particle density in June.

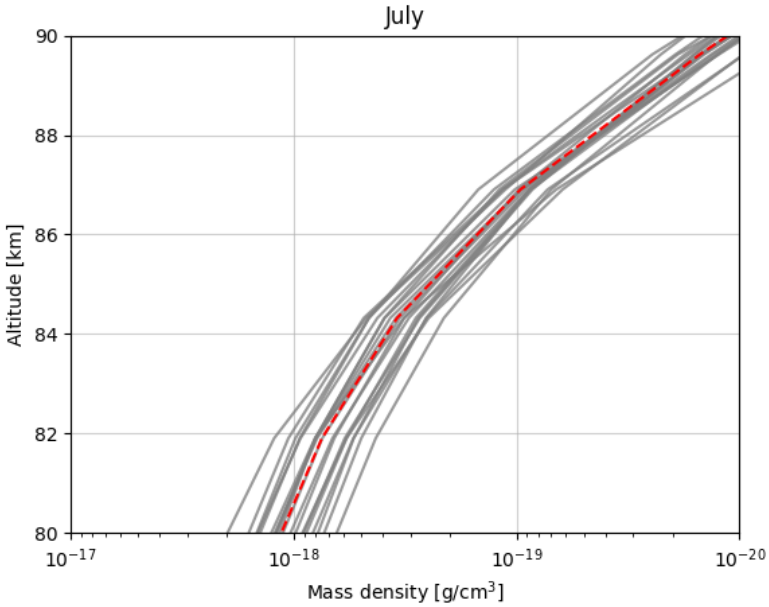

Figure 5.5: Similar results to Figure 5.4 presented in mass density and only for July.

In an effort to compare our results with literature, we consider the work done by Bardeen et al. [2008]. In the upper panel in Figure 4.1 at 70°N it appears that the number density has a peak of about 1000 /cm^3 just before 90 km. Both above and below this peak, the number density is around 500 /cm^3. Bardeen et al. [2008] state that due to the meridional circulations' relatively rapid transport of MSPs away from the summer mesopause, MSPs larger than 1 nm cannot quickly form, and most of the MSPs in the summer mesopause are 1 nm and smaller. Thus, the MSP number density in the summer mesopause would be relatively low compared to the winter mesopause. As heavier MSPs is less influenced by the mesospheric winds we expect most of the larger coagulated MSPs to be situated at lower altitudes, as seen in Figure 5.3. This is also seen in Figure 5.2, where the heavier MSPs generally have a lower number density than the lighter MSPs in the 80–90 km altitude region. By directly comparing Figure 4.1 to Figure 5.4 it appears that our results show a lower number density of about a factor of 10^2–10^4 depending on altitude. The peak in number density just before 90 km found in Figure 4.1 is not present in Figure 5.4, where the number density continuously decrease between 80 and 90 km.

The lower panel in Figure 4.1 again shows a similar peak around 90 km to that of the upper panel. As previously mentioned, due to the rapid transport of MSPs away from the summer mesopause, the residual MSPs left are of a smaller size and thus descend at slower rates. This is then shown as an increase in mass density in this region (lower panel in Figure 4.1). The authors however, note

that this increase is smaller than the variations in the last seven years of the control simulation. Looking at Figure 5.5 we see a clear continuous decrease of about two orders between 80 and 90 km, without a peak in densities around 90 km. In general, we see a difference of about 10^1–10^3 g/cm^3 less compared to Figure 4.1. According to Bardeen et al. [2008] the relation between meteoric influx and number density of larger particles (> 1 nm) are nonlinear, and an increase in meteoric influx by factor of 2 results in an 8-fold increase in number density. It is possible that the difference in our results compared to Bardeen et al. [2008] can be attributed to different meteoric influxes of the model runs.

5.3 MSP collection estimates with MESS

In this section we present the result on our estimates for sampling of MSPs with the MESS instrument. We have limited our analysis to June as this seems to be the most feasible month to perform the experiment considering MSP densities. Previously we have focused on the altitudes from 80 to 90 km. We have now extended our analysis to include estimates up to 95 km, as to see what effects this could have on the sampling process. Additionally, we show results from particles bigger than 10 nm. We assume the collection efficiency of MSPs bigger than 10 nm to be 100% at all altitudes. As previously mentioned, MSP sizes that appear to have less than 1 impact $/\text{cm}^2$ are assumed to not be collected.

We first present case of the collection efficiency for all MSPs being 100% at all times (Figure 5.6). The MSP sizes follow an apparent trend of the smaller they are, the more MSPs are collected. The biggest MSP to be collected are on the size of 16 nm, and starts at an altitude of 92 km. Sizes less than 2.54 nm seem to be collected already at 80 km. Below 90 km it appears that mostly MSPs with sizes 10 nm and less have the possibility to be collected. The total amount of collected particles at 95 km seem to be on the order of 10^7 $/\text{cm}^2$. Further, in Figure 5.7 we present the results of the collection estimates with a collection efficiency according to Tables 4.3 and 4.2. Since the actual rocket speed of MXD2 is uncertain, we show result for rocket speeds of 800 and 1000 m.s^{-1}.

In the case of the 1000 m.s^{-1} rocket speed, our analysis show no MSPs are collected before 82 km. At 82 km it appears to only be MSPs with sizes between 2.5 and 4 nm that are collected, followed by 4 nm MSPs being first collected at 84 km. As the size increase, the altitude at which they are starting to impact the collection surface increase, with the 16 nm size starting at 92 km. In the case of a rocket speed of 800 m.s^{-1}, the 2.54 nm size now seem to be collected at 82 km instead of 86 km. Size bins 2.54, 2.016 and 1.6 nm are still collected from 86 km and up. Before 86 km, the collection efficiency is zero, and no MSPs are collected. The profile seem to follow the similar trend to

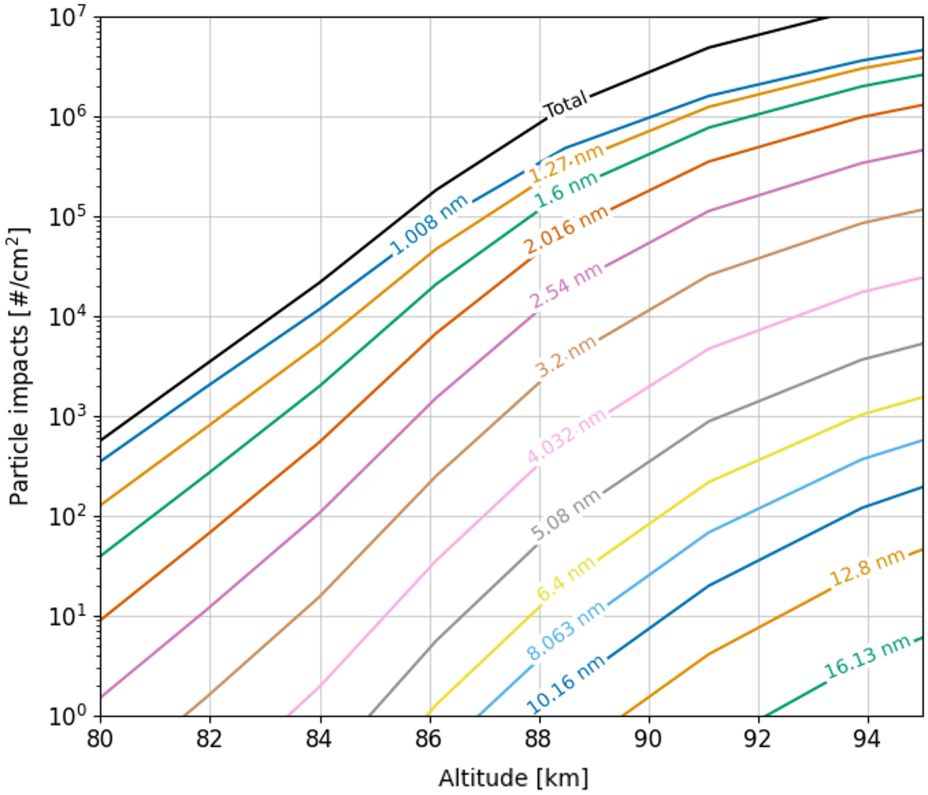

Figure 5.6: Estimates of the cumulative amount of sampled pure meteoric smoke particles for sampling attempts during June with the MESS instrument. We assume that MESS starts its sampling process at 80 km and end at 95 km. The collection efficiency is fixed at 100% throughout the sampling period.

Figure 5.6, where the bigger the MSPs are, the less is collected. The exception is for the two smallest particle bins, 1.008 and 1.27 nm. Here it seems to be more 1.27 nm MSPs collected than 1.008 nm in the altitude range 91 to 95 km. Past 95 km, the profiles start to flatten out and only increase about two orders from 95 to 150 km. By ending the sampling process at 105 km, the estimated amount of collected particles are on the order of 10^8 /cm^2.

Lastly, we present the total accumulated mass per square centimeter between 80 and 95 km for both rocket speeds in Figure 5.8. We do this in an attempt to further compare our results with previous estimates on similar results. Again we assume spherical particles with a material density of 2 g/cm^3.

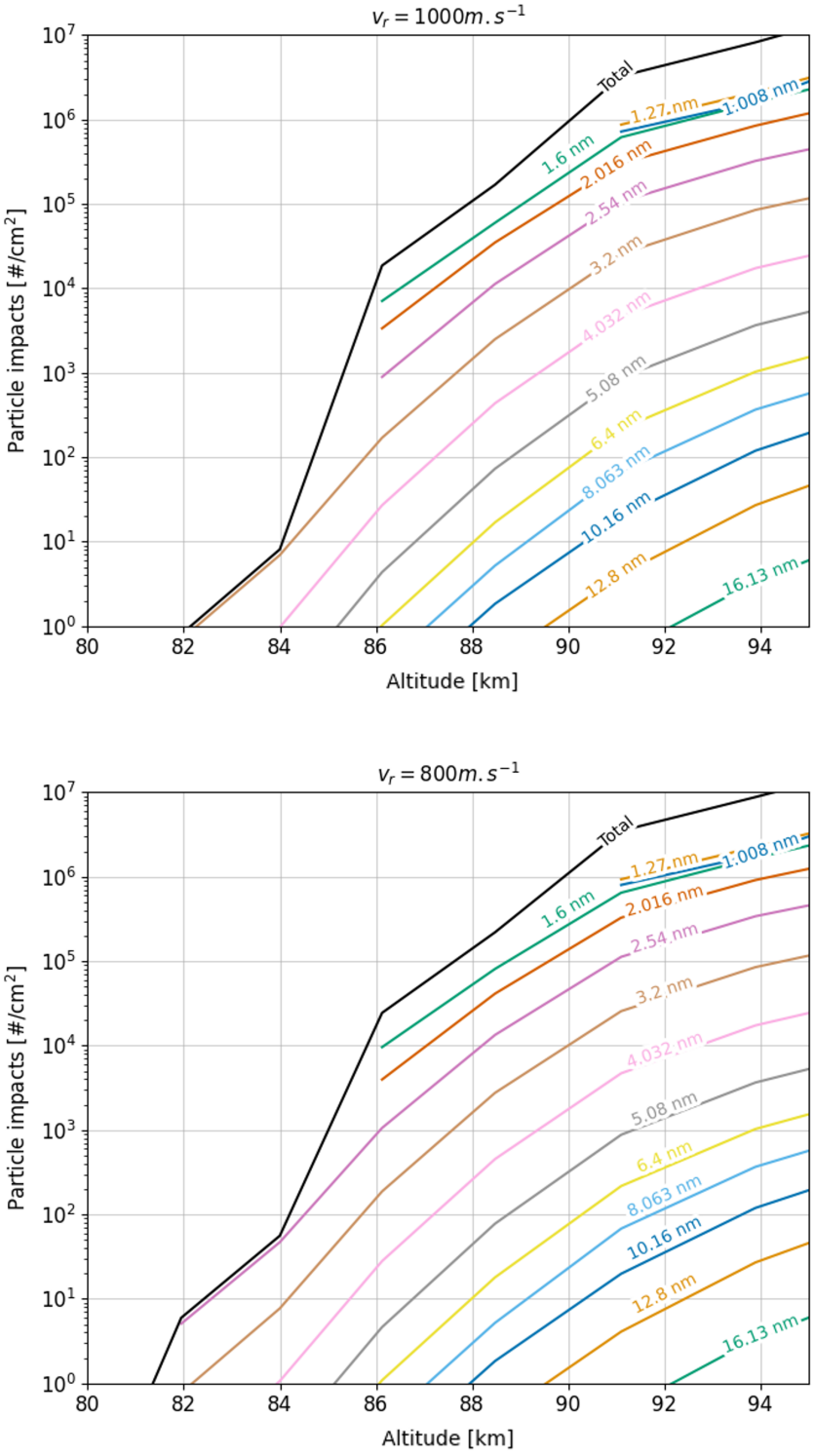

Figure 5.7: Estimates of the cumulative amount of sampled MSP for sampling attempts with the MESS instrument during a June campaign. We assume that MESS starts its sampling process at 80 km with a rocket speed of v_r = 1000 and 800 m.s^{-1}

5.3.1 Discussion

When starting the collection process at 80 km and ending at 90 km we can expect, based on our analysis, to collect a total amount of MSPs on the order of 10^6 /cm^2. By ending the collection process at 95 km instead, it increases the total amount of collected MSPs to an order of 10^7 /cm^2. Sub 1.6 nm MSPs appears to have insufficient momentum to penetrate the internal air pressure of MESS and reach the collection area before 91 km. This is due to the decrease in ambient air pressure with altitude. The slower the rocket speed is, the less the internal air pressure of MESS is, and more MSPs can reach the collection surface. This is apparent when comparing the 2.54 nm size bin for the two rockets speeds analysed. In general, we see that the rocket speed mostly alter the amount of collected particles below 86 km. Thus, it appears that the amount of collected MSPs are mostly influenced by the internal air pressure below 86 km. For a rocket speed of 1000 m.s^{-1}, MSPs with size 2.54 nm and smaller appear to be stopped below 86 km. For the MSP size bin 3.2 nm we see that their momentum can overcome the internal air pressure of MESS, but their number density is too low for there to be more than one particle per square centimeter on the collection surface until 84 km. This follows for all the larger particles. For size bins 12.8 and 16.13 nm, the collection efficiency is always 100%, thus the lack of particles before 90 km is due to the low number density.

As the MESS instrument is expected to collect ice particles as well, it is important to start the sampling processes at the correct time such that MESS is in full operational mode while passing through the ice particle layer. Even thought our analysis show no MSPs are collected before around 82 km, in order to optimize the collection of ice particles, MESS should be fully open when passing 80 km, based on the typical altitude of NLC and PMSE. As the ice particles are generally bigger than MSPs they will most likely have enough momentum to overcome the internal air pressure of MESS.

Pineau et al. [2023] estimated the total collected mass of MESS between 80 and 90 km for pure MSP and 82 to 85 km for ice particles. The authors used a MSP number density profile from Baumann et al. [2013], hence our MSP density profiles are from two separate sources. They find that for rocket speeds 800, 1000 and 1200 m.s^{-1}, the total amount of MSP mass collected is on the order of 10^{13}–10^{15} amu/mm^2. From Figure 5.8 we see that the final amount of collected mass with a sampling distance of 10 km is on the order of 10^{10} amu/cm^2 or 10^8 amu/mm^2 for both rocket speeds. Comparing to Pineau et al. [2023], it appears that our collected mass estimates is around 10^5–10^7 amu/mm^2 less. If we expand the sampling distance to 15 km, the collected mass appear to increase with about one order. In general, it appears that our estimates on MSP densities are significantly lower than previously published results. As mentioned, this could potentially be due to a lower meteoric mass influx, and other general uncertainties in the model assumptions. Nevertheless, the results show that under the assumptions used in this analysis, we can expect to collect

a substantial amount of pure MSPs when sampling from 80 to 95 km.

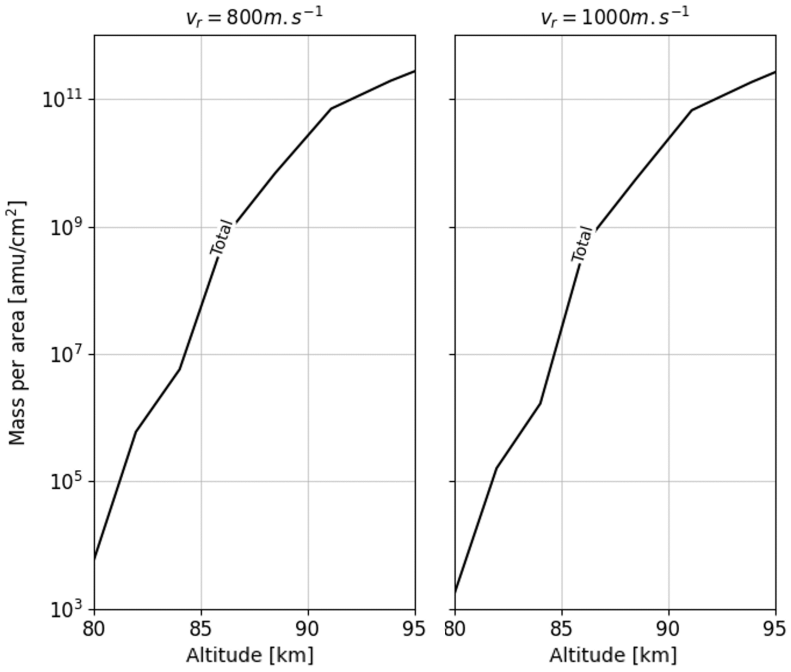

Figure 5.8: Estimates for the cumulative amount of collected mass for MSP sizes between 1 and 10 nm. The profiles are the same as Figure 5.8 but in the unit of atomic mass unit per square centimeter.

6

Conclusion

The goal of this thesis was to investigate the expected MSP densities in the mesopause region during the MAXIDUSTY-2 rocket campaign. We have used data from the global atmospheric model simulations WACCM/CARMA, in an attempt to investigate the apparent MSP conditions and variations that can be expected during the rocket campaign. Additionally, we provide estimates on the amount of MSP which can be expected to be collected by the MESS instruments during certain conditions. WACCM/CARMA models the global MSP transportation throughout the atmosphere based on a yearly meteor influx. The MSP size bins range from 0.2–104 nm radii, where we mostly consider MSPs in the 1–10 nm range due to the collection efficiencies of MESS.

The monthly and yearly variations in MSP densities have been investigated for June, July and August. In general, we expect the mesospheric circulation patterns to transport MSPs from the summer pole to the winter pole. Thus, the polar summer mesopause are excepted to show lower densities of MSP then the polar winter mesopause. Our analysis showed the opposite case, where the polar summer mesopause had a higher density of MSPs for the 1–10 nm size interval than the winter, specifically June and July. June also appeared to be the month, with the highest MSP density between 80 and 90 km out of the candidate months. As the MESS instrument is designed with the idea of increasing the likelihood of collected MSPs through both pure and ice embedded MSPs, a high as possible MSP density would prove beneficial. Thus, we offer the suggestion of June being the campaign month for the MXD2 rocket.

The other part of our analysis regards the estimates on the MSP collection capability of MESS. The MSPs were assumed to be spherical particles with a

material density of 2 g/cm^3, with June number densities between 10^{-1} – 10^1 $/cm^3$. We extended the analysis to 95 km, to investigate the possibility of increasing the sampling area. The collection efficiencies for MESS were found by Pineau et al. [2023]. The analysis showed that the rocket speed influenced the collection amount mostly below 86 km. For a rocket speed of 800 m.s^{-1}, the total amount of collected particles on the collection surface after sampling from 80–95 km, were on the order of 10^7 $/cm^2$ or 10^{11} g/cm^2. The final mass on the collection surface for a rocket speed of 1000 m.s^{-1} were on a similar order as the 800 m.s^{-1} case. However, the collection of MSPs in the size bin 2.54 nm starts at a higher altitude, possibly due to the increased internal air pressure of MESS, caused by the higher rocket speed. This might indicate that a lower rocket speed could benefit the MESS instrument, and a sampling area from 80–95 km would provide a sufficient amount of collected MSPs. Additionally, it is important to consider the mesospheric ice particle layers when determining the sampling area of MESS.

The results were compared to previous model simulations of WACCM/-CARMA. It appears that our MSP density estimates are generally a factor of 10^2 – 10^4 lower compared to the simulations done by Bardeen et al. [2008]. A considerable uncertainty in the analysis are the unconfirmed meteoric source function. The meteoric source function directly influence the amount of MSPs in the atmosphere, and the comparison to Bardeen et al. [2008] might indicate that our simulation had a smaller amount of meteoric influx. Other uncertainties in the model assumptions and atmospheric conditions should be considered.

Regarding future research, it could prove beneficial to investigate similar regions and conditions under varying meteoric influxes. This could assist in further understanding the fluctuations and distributions of MSP densities in the mesosphere. The future results from the MXD2 rocket campaign could potentially be compared to MSP distribution models in an effort to assist in the development of these models. Lastly, a similar analysis as done in this thesis should be performed for mesospheric ice particles in order to further understand their variations and distributions in preparations for the MXD2 rocket campaign.

Bibliography

D. Andrews. *An Introduction to Atmospheric Physics*. An Introduction to Atmospheric Physics. Cambridge University Press, 2000. ISBN 9780521629584.

T. Antonsen and O. Havnes. On the detection of mesospheric meteoric smoke particles embedded in noctilucent cloud particles with rocket-borne dust probes. *Review of Scientific Instruments*, 86(3):033305, 03 2015. ISSN 0034-6748. doi: 10.1063/1.4914394.

T. Antonsen, O. Havnes, and I. Mann. Estimates of the size distribution of meteoric smoke particles from rocket-borne impact probes. *Journal of Geophysical Research: Atmospheres*, 122(22):12,353–12,365, 2017. doi: https://doi.org/10.1002/2017JD027220.

S. M. Bailey, B. Thurairajah, M. E. Hervig, D. E. Siskind, J. M. Russell, and L. L. Gordley. Trends in the polar summer mesosphere temperature and pressure altitude from satellite observations. *Journal of Atmospheric and Solar-Terrestrial Physics*, 220:105650, 2021. ISSN 1364-6826. doi: https://doi.org/10.1016/j.jastp.2021.105650.

C. G. Bardeen, O. B. Toon, E. J. Jensen, D. R. Marsh, and V. L. Harvey. Numerical simulations of the three-dimensional distribution of meteoric dust in the mesosphere and upper stratosphere. *Journal of Geophysical Research: Atmospheres*, 113(D17), 2008. doi: https://doi.org/10.1029/2007JD009515.

C. Baumann. Influences of meteoric aerosol particles on the lower ionosphere. *Doctoral dissertation, Ludwig-Maximilians-Universität München*, 2016.

C. Baumann, M. Rapp, A. Kero, and C.-F. Enell. Meteor smoke influences on the d-region charge balance – review of recent in situ measurements and one-dimensional model results. *Annales Geophysicae*, 31:2049–2062, 2013.

A. Brekke. Physics of the upper polar atmosphere. *Springer-Verlag Berlin and Heidelberg GmbH Co. K*, Springer Atmospheric Sciences, 2012.

A. W. Brewer. Evidence for a world circulation provided by the measurements of helium and water vapour distribution in the stratosphere. *Quarterly Journal of the Royal Meteorological Society*, 75(326):351–363, 1949. doi: https://doi.org/10.1002/qj.49707532603.

J. S. A. Brooke, W. Feng, J. D. Carrillo-Sánchez, G. W. Mann, A. D. James, C. G. Bardeen, L. Marshall, S. S. Dhomse, and J. M. C. Plane. Meteoric smoke deposition in the polar regions: A comparison of measurements with global atmospheric models. *Journal of Geophysical Research: Atmospheres*, 122(20): 11,112–11,130, 2017. doi: https://doi.org/10.1002/2017JD027143.

J. G. Charney and P. G. Drazin. Propagation of planetary-scale disturbances from the lower into the upper atmosphere. *Journal of Geophysical Research (1896-1977)*, 66(1):83–109, 1961. doi: https://doi.org/10.1029/JZ066i001p00083.

G. M. B. Dobson and H. S. W. Massey. Origin and distribution of the polyatomic molecules in the atmosphere. *Proceedings of the Royal Society of London. Series A. Mathematical and Physical Sciences*, 236(1205):187–193, 1956. doi: 10.1098/rspa.1956.0127.

M. Friedrich, K. Torkar, U.-P. Hoppe, T.-A. Bekkeng, A. Barjatya, and M. Rapp. Multi-instrument comparisons of d-region plasma measurements. *Annales Geophysicae*, 31:135–144, 01 2013. doi: 10.5194/angeo-31-135-2013.

M. Gadsen and W. Schroder. Noctilucent clouds. *Springer Verlag Springer Series on Physics Chemistry Space*, 18, Jan. 1989.

T. Gunnarsdottir. Charging effects and detection of mesospheric dust with the instrument spid on the g-chaser rocket. *Master thesis, UiT Norges arktiske universitet*, 2019.

T. L. Gunnarsdottir, I. Mann, W. Feng, D. R. Huyghebaert, I. Haeggstroem, Y. Ogawa, N. Saito, S. Nozawa, and T. D. Kawahara. Influence of meteoric smoke particles on the incoherent scatter measured with eiscat vh. *Annales Geophysicae Discussions*, 2023:1–22, 2023. doi: 10.5194/angeo-2023-29.

O. Havnes and L. I. Næsheim. On the secondary charging effects and structure of mesospheric dust particles impacting on rocket probes. *Annales Geophysicae*, 25(3):623–637, 2007. doi: 10.5194/angeo-25-623-2007.

O. Havnes, J. Trøim, T. Blix, W. Mortensen, L. I. Næsheim, E. Thrane, and T. Tønnesen. First detection of charged dust particles in the earth's mesosphere. *Journal of Geophysical Research: Space Physics*, 101(A5):10839–10847, 1996.

doi: https://doi.org/10.1029/96JA00003.

O. Havnes, T. Antonsen, T. Hartquist, Fredriksen, and J. Plane. The tromsø programme of in situ and sample return studies of mesospheric nanoparticles. *Journal of Atmospheric and Solar-Terrestrial Physics*, 127:129–136, 2015. ISSN 1364-6826. doi: https://doi.org/10.1016/j.jastp.2014.09.010. Layered Phenomena in the Mesopause Region.

C. J. Heale and J. B. Snively. Gravity wave propagation through a vertically and horizontally inhomogeneous background wind. *Journal of Geophysical Research: Atmospheres*, 120(12):5931–5950, 2015. doi: https://doi.org/10.1002/2015JD023505.

J. Hedin, F. Giovane, T. Waldemarsson, J. Gumbel, J. Blum, R. M. Stroud, L. Marlin, J. Moser, D. E. Siskind, K. Jansson, R. W. Saunders, M. E. Summers, P. Reissaus, J. Stegman, J. M. Plane, and M. Horányi. The magic meteoric smoke particle sampler. *Journal of Atmospheric and Solar-Terrestrial Physics*, 118:127–144, 2014. ISSN 1364-6826. doi: https://doi.org/10.1016/j.jastp.2014.03.003.

M. E. Hervig, L. L. Gordley, L. E. Deaver, D. E. Siskind, M. H. Stevens, J. M. Russell III, S. M. Bailey, L. Megner, and C. G. Bardeen. First satellite observations of meteoric smoke in the middle atmosphere. *Geophysical Research Letters*, 36(18), 2009. doi: https://doi.org/10.1029/2009GL039737.

M. E. Hervig, L. E. Deaver, C. G. Bardeen, J. M. Russell, S. M. Bailey, and L. L. Gordley. The content and composition of meteoric smoke in mesospheric ice particles from sofie observations. *Journal of Atmospheric and Solar-Terrestrial Physics*, 84-85:1–6, 2012. ISSN 1364-6826. doi: https://doi.org/10.1016/j.jastp.2012.04.005.

M. E. Hervig, J. M. C. Plane, D. E. Siskind, W. Feng, C. G. Bardeen, and S. M. Bailey. New global meteoric smoke observations from sofie: Insight regarding chemical composition, meteoric influx, and hemispheric asymmetry. *Journal of Geophysical Research: Atmospheres*, 126(13):e2021JD035007, 2021. doi: https://doi.org/10.1029/2021JD035007. e2021JD035007 2021JD035007.

J. Holton. *An Introduction to Dynamic Meteorology*. International Geophysics. Elsevier Science, 2004. ISBN 9780123540157.

D. M. Hunten, R. P. Turco, and O. B. Toon. Smoke and dust particles of meteoric origin in the mesosphere and stratosphere. *Journal of Atmospheric Sciences*, 37(6):1342 – 1357, 1980. doi: https://doi.org/10.1175/1520-0469(1980)037<1342:SADPOM>2.0.CO;2.

K. S. Jacobsen, A. Pedersen, J. I. Moen, and T. A. Bekkeng. A new langmuir probe concept for rapid sampling of space plasma electron density. *Measurement Science and Technology*, 21:085902, 2010.

B. Karlsson and T. G. Shepherd. The improbable clouds at the edge of the atmosphere. *Physics Today*, 71(6):30–36, 06 2018. ISSN 0031-9228. doi: 10.1063/PT.3.3946.

M. Kassa, M. Rapp, T. W. Hartquist, and O. Havnes. Secondary charging effects due to icy dust particle impacts on rocket payloads. *Annales Geophysicae*, 30 (3):433–439, 2012. doi: 10.5194/angeo-30-433-2012.

S. G. Love and D. E. Brownlee. A direct measurement of the terrestrial mass accretion rate of cosmic dust. *Science*, 262(5133):550–553, 1993. doi: 10.1126/science.262.5133.550.

I. Mann, S. V. Olsen, Y. Eilertsen, H. Trollvik, A. Pineau, S. S. Palinkas, T. L. Gunnarsdottir, H. L. Greaker, Å. Fredriksen, and A. Spincher. Mesospheric dust studies with mxd2. *ESA SP 2022*, 2022. ISSN 0379-6566.

L. Megner and J. Gumbel. Charged meteoric particles as ice nuclei in the mesosphere: Part 2: A feasibility study. *Journal of Atmospheric and Solar-Terrestrial Physics*, 71(12):1236–1244, 2009. ISSN 1364-6826. doi: https://doi.org/10.1016/j.jastp.2009.05.002.

L. Megner, M. Rapp, and J. Gumbel. Distribution of meteoric smoke ndash; sensitivity to microphysical properties and atmospheric conditions. *Atmospheric Chemistry and Physics*, 6(12):4415–4426, 2006. doi: 10.5194/acp-6-4415-2006.

L. Megner, D. E. Siskind, M. Rapp, and J. Gumbel. Global and temporal distribution of meteoric smoke: A two-dimensional simulation study. *Journal of Geophysical Research: Atmospheres*, 113(D3), 2008. doi: https://doi.org/10.1029/2007JD009054.

C. Nappo. *An Introduction to Atmospheric Gravity Waves*. ISSN. Elsevier Science, 2002. ISBN 9780080491660.

D. Nesvorný, P. Jenniskens, H. F. Levison, W. F. Bottke, D. Vokrouhlický, and M. Gounelle. Cometary origin of the zodiacal cloud and carbonaceous micrometeorites. implications for hot debris disks. *The Astrophysical Journal*, 713:816 – 836, 2009.

A. Pineau, H. Trollvik, S. Olsen, Y. Eilertsen, and I. Mann. Simulations of the

collection of mesospheric dust particles with rocket instrument. *EGUsphere*, 2023:1–26, 2023. doi: 10.5194/egusphere-2023-2762.

J. Plane, F. Wuhu, and E. Dawkins. The mesosphere and metals: Chemistry and changes. *Chemical reviews*, 115, 03 2015. doi: 10.1021/cr500501m.

J. M. Plane, R. W. Saunders, J. Hedin, J. Stegman, M. Khaplanov, J. Gumbel, K. A. Lynch, P. J. Bracikowski, L. J. Gelinas, M. Friedrich, S. Blindheim, M. Gausa, and B. P. Williams. A combined rocket-borne and ground-based study of the sodium layer and charged dust in the upper mesosphere. *Journal of Atmospheric and Solar-Terrestrial Physics*, 118:151–160, 2014. ISSN 1364-6826. doi: https://doi.org/10.1016/j.jastp.2013.11.008. Smoke and Ice in the Mesosphere.

J. M. C. Plane. Atmospheric chemistry of meteoric metals. *Chemical Reviews*, 103(12):4963–4984, 2003. doi: 10.1021/cr0205309. PMID: 14664639.

J. M. C. Plane. Cosmic dust in the earth's atmosphere. *Chem. Soc. Rev.*, 41: 6507–6518, 2012. doi: 10.1039/C2CS35132C.

R. A. Plumb. Stratospheric transport. *Journal of the Meteorological Society of Japan. Ser. II*, 80(4B):793–809, 2002. doi: 10.2151/jmsj.80.793.

M. Rapp and F.-J. Lübken. Polar mesosphere summer echoes (pmse): Review of observations and current understanding. *Atmospheric Chemistry and Physics*, 4(11/12):2601–2633, 2004. doi: 10.5194/acp-4-2601-2004.

M. Rapp, J. Hedin, I. Strelnikova, M. Friedrich, J. Gumbel, and F.-J. Lübken. Observations of positively charged nanoparticles in the nighttime polar mesosphere. *Geophysical Research Letters*, 32(23), 2005. doi: https://doi.org/10.1029/2005GL024676.

M. Rapp, I. Strelnikova, and J. Gumbel. Meteoric smoke particles: Evidence from rocket and radar techniques. *Advances in Space Research*, 40(6):809–817, 2007. ISSN 0273-1177. doi: https://doi.org/10.1016/j.asr.2006.11.021.

M. Rapp, I. Strelnikova, B. Strelnikov, P. Hoffmann, M. Friedrich, J. Gumbel, L. Megner, U.-P. Hoppe, S. Robertson, S. Knappmiller, M. Wolff, and D. R. Marsh. Rocket-borne in situ measurements of meteor smoke: Charging properties and implications for seasonal variation. *Journal of Geophysical Research: Atmospheres*, 115(D1), 2010. doi: https://doi.org/10.1029/2009JD012725.

J. H. Richter, F. Sassi, Garcia, R.R., Matthes, K., and Ficher, C.A. Dynamics of the middle atmosphere as simulated by the whole atmosphere community

climate model, version 3 (waccm3). *Journal Of Geophysical Research*, 113, 2008. doi: 10.1029/2007JD009269.

H. Roscoe. The brewer–dobson circulation in the stratosphere and mesosphere – is there a trend? *Advances in Space Research*, 38(11):2446–2451, 2006. ISSN 0273-1177. doi: https://doi.org/10.1016/j.asr.2006.02.078. Middle and Upper Atmospheres, Active Experiments, and Dusty Plasmas.

R. W. Saunders and J. M. Plane. A laboratory study of meteor smoke analogues: Composition, optical properties and growth kinetics. *Journal of Atmospheric and Solar-Terrestrial Physics*, 68(18):2182–2202, 2006. ISSN 1364-6826. doi: https://doi.org/10.1016/j.jastp.2006.09.006.

R. W. Saunders and J. M. C. Plane. A photo-chemical method for the production of olivine nanoparticles as cosmic dust analogues. *Icarus*, 212:373–382, 2011.

P. E. Sheese, E. J. Llewellyn, R. L. Gattinger, A. E. Bourassa, D. A. Degenstein, N. D. Lloyd, and I. C. McDade. Mesopause temperatures during the polar mesospheric cloud season. *Geophysical Research Letters*, 38(11), 2011. doi: https://doi.org/10.1029/2011GL047437.

T. G. Shepherd. Transport in the middle atmosphere. *Journal of the Meteorological Society of Japan. Ser. II*, 85B:165–191, 2007. doi: 10.2151/jmsj.85B.165.

B. Strelnikov, M. Rapp, and F.-J. Lübkin. *In-situ density measurements in the mesosphere/lower thermosphere region with the TOTAL and CONE instruments*, pages 1–11. 01 2013. ISBN 9784887041608. doi: 10.5047/aisi.001.

I. Strelnikova, M. Rapp, S. Raizada, and M. Sulzer. Meteor smoke particle properties derived from arecibo incoherent scatter radar observations. *Geophysical Research Letters*, 34(15), 2007. doi: https://doi.org/10.1029/2007GL030635.

O. B. Toon, R. P. Turco, P. Hamill, C. S. Kiang, and R. C. Whitten. A one-dimensional model describing aerosol formation and evolution in the stratosphere: Ii. sensitivity studies and comparison with observations. *Journal of Atmospheric Sciences*, 36(4):718 – 736, 1979. doi: https://doi.org/10.1175/1520-0469(1979)036<0718:AODMDA>2.0.CO;2.

H. Trollvik, T. L. Gunnarsdottir, I. Mann, S. V. Olsen, E. Restad, T. Antonsen, Å. Fredriksen, Y. Eilertsen, O. Havnes, R. H. Hansen, M. Floer, A. Bjørk, Christopher, Bootby, and R. Latteck. Simulations of the smoke particle impact detector(spid) and observations during the g-chaser rocket campaign. 2019.

R. P. Turco, P. Hamill, O. B. Toon, R. C. Whitten, and C. S. Kiang. A one-dimensional model describing aerosol formation and evolution in the stratosphere: I. physical processes and mathematical analogs. *Journal of Atmospheric Sciences*, 36(4):699 – 717, 1979. doi: https://doi.org/10.1175/1520-0469(1979)036<0699:AODMDA>2.0.CO;2.

S. Zhang and W. Tian. The effects of stratospheric meridional circulation on surface pressure and tropospheric meridional circulation. *Climate Dynamics*, 53, 12 2019. doi: 10.1007/s00382-019-04968-x.

7

Appendix

This appendix contains the Python 3.10.4 script for calculating and displaying the results presented in chapter 5.

```
import numpy as np
import matplotlib
import matplotlib.pyplot as plt
import matplotlib.ticker as ticker
import xarray as xr
from metpy.calc import sigma_to_pressure,
    geopotential_to_height
from metpy.units import units
import pandas as pd
import seaborn as sns
from dust_sizes_file import data_dust_size_1_to_8nm,
    data_dust_size
from labellines import labelLine, labelLines


def data_dust_size(year, month, lat, lon, dust_size):
    """
    :param year: model year
    :param month: model month
    :param lat: latitude
    :param lon: longitude
    :param dust_size: size bin for the dust particles
    :return: altitude, pressure, temprature, Total number
    density dust, estimate of the total number density, number
    density of the particular dust size ibn
    """
```

```
    global dust_rad, dust_sizes, density_air, sum_ND, altitude
    path = "DATA PATH"
    df = xr.open_dataset(path + "WACCM_METALS_CARMA_MSP-00" +
str(year) + "-" + str(month) + ".nc")  # data import

    # finding the closes datapoint to the requested latitude
and longitude
    close_lon = min(df.lon.values, key=lambda x: abs(x - lon))
    close_lat = min(df.lat.values, key=lambda x: abs(x - lat))
    lon_index, = np.where(df.lon.values == close_lon)
    lat_index, = np.where(df.lat.values == close_lat)

    geopotential_height = np.zeros(len(df.lev))  # altitude in
geopotential height
    pressure = np.zeros(len(df.lev))  # altitude pressure
    temp = np.zeros(len(df.lev))  # atmospheric temperature
    dust01, dust02, dust03, dust04, dust05, dust06, dust07,
dust08, dust09, dust10, dust11, dust12, dust13, dust14, \
    dust15, dust16, dust17, dust18, dust19, dust20, dust21,
dust22, dust23, dust24, dust25, dust26, dust27, dust28 = \
        np.zeros(len(df.lev))  # mass mixing ratio [kg/kg] for
radii = 0.2 to 102.4 nm
    dustND = np.zeros(len(df.lev))  # total number density [#/
cm3]
    sum_ND = np.zeros(len(dust01))
    dust_sizes = [0.2, 0.252, 0.3175, 0.4, 0.5040, 0.6350, 0.8,
 1.008, 1.270, 1.6, 2.016, 2.540, 3.200, 4.032,
                  5.080, 6.400, 8.063, 10.16, 12.80, 16.13,
20.32, 25.60, 32.25, 40.64, 51.20, 64.51, 81.27, 102.4]
    dust_rad = [dust01, dust02, dust03, dust04, dust05, dust06,
 dust07, dust08, dust09, dust10, dust11, dust12,
                dust13, dust14, dust15, dust16, dust17, dust18,
 dust19, dust20, dust21, dust22, dust23, dust24,
                dust25, dust26, dust27, dust28]

    # foo = df.parameter[time][altitude][latitude][longitude].
values
    for i in range(len(df.lev)):
        geopotential_height[i] = df.Z3[0][i][lat_index[0]][
lon_index[0]].values
        pressure[i] = df.lev[i].values
        for i, size_bin in enumerate(dust_rad):
            temp[i] = df.T[0][i][lat_index[0]][lon_index[0]].
values  # temperature
            size_bin = df.DUST01[0][i][lat_index[0]][lon_index
[0]].values  # Dust number density for each size bin
            ps = df.PS[0][lat_index[0]][lon_index[0]].values  #
 surface pressure

    altitude = geopotential_to_height(geopotential_height.
tolist() * (units.meter * units.meter) / (
            units.second * units.second))  # transform geo.pot
height to geo. height

```

```
60      R_s = 287.05  # specific gas constant for dry air [J/(kg K)
        ]
61      density_air = (pressure * 100) / (R_s * temp)  # [kg/m3]
62
63      for i in range(len(dust_sizes)):
64          # sum of all size bins
65          # convert kg/kg to #/cm3
66          mass_particle_for_sum = (4 / 3 * np.pi * (
67                  dust_sizes[i] * 1E-9) ** 3) * 2000  #
        dustVolume[m3] * dustDenisty of 2000[kg/m3]  = dustMass[kg]
68          number_density = dust_rad[i] * density_air /
        mass_particle_for_sum  # kg_a/kg_p * kg_a/m3 / kg_p =  #/m3
69          sum_ND += number_density
70
71          # same as for-loop above, but for the individual size
        bins
72      mass_particle = (4 / 3 * np.pi * (dust_sizes[dust_size] * 1
        E-9) ** 3) * 2000
73      number_density_dust = dust_rad[dust_size] * density_air /
        mass_particle
74
75      return altitude, pressure, temp, dustND, sum_ND,
        number_density_dust
76
77
78  def plot_func():
79      """
80      Plotting function of the MSP number densities per month.
81      Swap "months" with "years", to plot MSP number densities
        per year.
82
83      :return: None
84      """
85      years = ["13", "14", "15", "16", "17", "18", "19", "20", "
        21", "22"]
86      months = ["01", "02", "03", "04", "05", "06", "07", "08", "
        09", "10", "11", "12"]
87      months_txt = ["Jan", "Feb", "Mar", "Apr", "May", "Jun", "
        Jul", "Aug", "Sep", "Oct", "Nov", "Dec"]
88      dust_sizes = [0.2, 0.252, 0.3175, 0.4, 0.5040, 0.6350, 0.8,
         1.008, 1.270, 1.6, 2.016, 2.540, 3.200, 4.032,
89                    5.080, 6.400, 8.063]
90
91      # create dataframes for each dust size bin per month
92      plot_label = [f"{i}" for i in months]
93      N_r, N_r2, N_r3 = pd.DataFrame(columns=plot_label, index=[i
         for i in range(66)])
94
95      for i, j in enumerate(months):
96          # assigned the dfs' values
97          altitude, pressure, temp, dustND, sum_ND, col =
        data_dust_size("22", j, 69.6, 19.2, 7)
98          altitude, pressure, temp, dustND, sum_ND, col2 =
        data_dust_size("22", j, 69.6, 19.2, 10)
```

```
99          altitude, pressure, temp, dustND, sum_ND, col3 =
    data_dust_size("22", j, 69.6, 19.2, 12)
100         columes = [col, col2, col3]
101
102         for indx, df in enumerate([N_r, N_r2, N_r3]):
103             df[indx] = columes[indx]
104
105     # ----------PLOT--------------
106     with sns.husl_palette(n_colors=12, l=.5):
107
108         fig, (ax1, ax2, ax3) = plt.subplots(1, 3, sharey=True,
    sharex=False)
109
110         plt.rc('axes', labelsize=13)  # fontsize of the x and y
     labels
111         plt.rc('xtick', labelsize=13)  # fontsize of the x tick
     labels
112         plt.rc('ytick', labelsize=13)  # fontsize of the y tick
     labels
113         plt.gcf().set_tight_layout(True)
114
115         for i, j in enumerate(months):
116             # mark some months with markers
117             if j == "06":
118                 ax1.plot(N_r[j] / 1e6, altitude / 1e2, label=f"
    {months_txt[i]}", marker="x")
119                 ax2.plot(N_r2[j] / 1e6, altitude / 1e2, label=f
    "{months_txt[i]}", marker="x")
120                 ax3.plot(N_r3[j] / 1e6, altitude / 1e2, label=f
    "{months_txt[i]}", marker="x")
121             elif j == "07":
122                 ax1.plot(N_r[j] / 1e6, altitude / 1e2, label=f"
    {months_txt[i]}", marker="o")
123                 ax2.plot(N_r2[j] / 1e6, altitude / 1e2, label=f
    "{months_txt[i]}", marker="o")
124                 ax3.plot(N_r3[j] / 1e6, altitude / 1e2, label=f
    "{months_txt[i]}", marker="o")
125             elif j == "08":
126                 ax1.plot(N_r[j] / 1e6, altitude / 1e2, label=f"
    {months_txt[i]}", marker="d")
127                 ax2.plot(N_r2[j] / 1e6, altitude / 1e2, label=f
    "{months_txt[i]}", marker="d")
128                 ax3.plot(N_r3[j] / 1e6, altitude / 1e2, label=f
    "{months_txt[i]}", marker="d")
129             if j == "01" or "02" or "03" or "04" or "11" or "12
    ":
130                 ax1.plot(N_r[j] / 1e6, altitude / 1e2, label=f"
    {months_txt[i]}", linestyle="dotted")
131                 ax2.plot(N_r2[j] / 1e6, altitude / 1e2, label=f
    "{months_txt[i]}", linestyle="dotted")
132                 ax3.plot(N_r3[j] / 1e6, altitude / 1e2, label=f
    "{months_txt[i]}", linestyle="dotted")
133             else:
134                 ax1.plot(N_r[j] / 1e6, altitude / 1e2, label=f"
```

```
    {months_txt[i]}")
135                 ax2.plot(N_r2[j] / 1e6, altitude / 1e2, label=f
    "{months_txt[i]}")
136                 ax3.plot(N_r3[j] / 1e6, altitude / 1e2, label=f
    "{months_txt[i]}")
137
138         ax1.set_title(f"$r_d$ = {dust_sizes[7]} nm")
139         ax2.set_title(f"$r_d$ = {dust_sizes[10]} nm")
140         ax3.set_title(f"$r_d$ = {dust_sizes[12]} nm")
141         ax3.legend(loc="upper right")
142         ax1.grid(alpha=0.6)
143         ax2.grid(alpha=0.6)
144         ax3.grid(alpha=0.6)
145         ax1.set_xscale("log")
146         ax2.set_xscale("log")
147         ax3.set_xscale("log")
148         ax1.set_xlim(1e-4, 1)
149         ax2.set_xlim(0, 5)
150         ax3.set_xlim(0, 5)
151         ax1.set_ylim(60, 100)
152         ax1.set_xlim(1e-5, 1e-2)
153         ax2.set_xlabel("number density [#/cm$^3$]")
154         ax2.set_xlabel("number density $[\#/cm^3]$")
155         ax3.set_xlabel("number density $[\#/cm^3]$")
156         ax1.set_ylabel("altitude [km]")
157         plt.show()
158
159
160 def yearly_avg(year=str):
161     """
162     Calculating the yearly averaged dust number densities
163
164     :param year: which year to calcuate the mean of : str
165
166     :return: mean of total dust number densities, mean of the
    number densities of a specific dust size bin
167     """
168     global added_N_r
169     months = ["01", "02", "03", "04", "05", "06", "07", "08", "
    09", "10", "11", "12"]
170     added_N_r = 0.0
171     added_N_D = 0.0
172     for i in months:
173         altitude, pressure, temp, dustND, sum_ND, N_r,
    plot_label = data_dust_size(year, i, 69.6, 19.2, 0)
174         added_N_r += sum_ND
175         added_N_D += dustND
176     mean_N_D = added_N_D / 12
177     mean_N_r = added_N_r / 12
178
179     return mean_N_D, mean_N_r
180
181
182 def dust_collection_estimates():
```

```
183     years = ["13", "14", "15", "16", "17", "18", "19", "20", "
        21", "22"]
184     months = ["01", "02", "03", "04", "05", "06", "07", "08", "
        09", "10", "11", "12"]
185     months_txt = ["Jan", "Feb", "Mar", "Apr", "May", "Jun", "
        Jul", "Aug", "Sep", "Oct", "Nov", "Dec"]
186     dust_sizes = [1.008, 1.270, 1.6, 2.016, 2.540, 3.200,
        4.032, 5.080, 6.400, 8.063, 10.16, 12.80, 16.13, 20.32,
        25.60,
187                   32.25, 40.64, 51.20, 64.51, 81.27, 102.4]
188
189     vertical_steps = 66  # number of vertical model points
190     dust_size_bins_idx = range(7, 21)
191     # MESS specifications for funnel opening and collection
        surface
192     A_c = 2.545E-4  # m2
193     A_f = 19.635E-4  # m2
194
195     N_r_jun, N_r1_jun, N_r2_jun, N_r3_jun, N_r4_jun, N_r4_jun,
        N_r5_jun, N_r6_jun, N_r7_jun, N_r8_jun, N_r9_jun, \
196     N_r10_jun, N_r11_jun, N_r12_jun, N_r13_jun = np.zeros(range
        (vertical_steps))
197
198     N_r_list = [N_r_jun, N_r1_jun, N_r2_jun, N_r3_jun, N_r4_jun
        , N_r4_jun, N_r5_jun, N_r6_jun, N_r7_jun, N_r8_jun,
199                 N_r9_jun, N_r10_jun, N_r11_jun, N_r12_jun,
        N_r13_jun]
200
201     N_c1_june, N_c2_june, N_c3_june, N_c4_june, N_c5_june,
        N_c6_june, N_c7_june, N_c8_june, N_c9_june, N_c10_june, \
202     N_c11_june, N_c12_june, N_c13_june, N_c14_june = np.zeros(
        len(vertical_steps))
203
204     N_c_list = [N_c1_june, N_c2_june, N_c3_june, N_c4_june,
        N_c5_june, N_c6_june, N_c7_june, N_c8_june, N_c9_june,
205                 N_c10_june, N_c11_june, N_c12_june, N_c13_june,
         N_c14_june]
206
207     # Extracting number densities of specific dust size bins
208     for i, j in enumerate(dust_size_bins_idx):
209         altitude, pressure, temp, dustND, sum_ND, N_r_list[i] =
         data_dust_size("22", "07", 69.6, 19.2, j)
210
211         N_r_list[i] = N_r_list[i][7:27]  # limiting the
        vertical range to around 80 km to 95 km.
212
213     alt = altitude[::-1] / (units.meter)  # inverting the
        vertical coordinated
214     alt = alt[49:68] * 10  # liitng th altiutde to around 80 km
         to 95km and turing it into Pa
215     L = np.zeros(len(alt))
216
217     # Collection efficiencies for a rocket speed of 1000 m.s^-1
218     cr_1nm1000 = [0, 0, 0, 0.45]
```

```
219     cr_2nm1000 = [0, 0, 0, 0.7]
220     cr_3nm1000 = [0, 0, 0.34, 0.8]
221     cr_4nm1000 = [0, 0, 0.5, 0.86]
222     cr_5nm1000 = [0, 0, 0.59, 0.95]
223     cr_6nm1000 = [0, 0.45, 0.68, 1]
224     cr_7nm1000 = [0, 0.5, 0.76, 1]
225     cr_8nm1000 = [0.37, 0.54, 0.78, 1]
226     cr_9nm1000 = [0.45, 0.59, 0.80, 1]
227     cr_10nm1000 = [0.5, 0.63, 0.82, 1]
228
229    # Collection efficiencies for a rocket speed of 800 m.s^-1
230     cr_1nm800 = [0, 0, 0, 0.5]
231     cr_2nm800 = [0, 0, 0, 0.75]
232     cr_3nm800 = [0, 0, 0.46, 0.84]
233     cr_4nm800 = [0, 0, 0.59, 0.93]
234     cr_5nm800 = [0, 0.44, 0.70, 1]
235     cr_6nm800 = [0, 0.5, 0.75, 1]
236     cr_7nm800 = [0.43, 0.55, 0.79, 1]
237     cr_8nm800 = [0.48, 0.62, 0.83, 1]
238     cr_9nm800 = [0.5, 0.68, 0.85, 1]
239     cr_10nm800 = [0.55, 0.72, 0.82, 1]
240
241     cr_list800 = [cr_1nm800, cr_2nm800, cr_3nm800, cr_4nm800,
    cr_5nm800, cr_6nm800, cr_7nm800, cr_8nm800, cr_9nm800,
242                 cr_10nm800]
243     cr_list1000 = [cr_1nm1000, cr_2nm1000, cr_3nm1000,
    cr_4nm1000, cr_5nm1000, cr_6nm1000, cr_7nm1000, cr_8nm1000,
     cr_9nm1000,
244                 cr_10nm1000]
245
246     for i in range(len(alt)):
247         L[i] = alt[i] - alt[i - 1]
248         L[0] = 0
249
250         for indx, list in enumerate(N_c_list):
251             # calculating the collection estimates
252             list[indx] = N_c1_june[i - 1] + (A_f * L[i] *
    N_r_jun[i] / A_c) * (4 / 3 * np.pi *
253
                     (dust_sizes[indx] * 1E-9) ** 3) * 2000
254
255     # Applying the collection efficiencies, size bins larger
    than indx 10 have 100% coll.eff
256     for i in range(len(N_c1_june)):
257         if i <= 1:
258             for indx, list in enumerate(N_r_list[0:9]):
259                 list[indx] *= cr_list800[indx][0]
260
261         if i == 2 or i == 3:
262             for indx, list in enumerate(N_r_list[0:9]):
263                 list[indx] *= cr_list800[indx][1]
264
265         if i == 4 or i == 5:
266             for indx, list in enumerate(N_r_list[0:9]):
```

```
267                 list[indx] *= cr_list800[indx][2]
268
269             elif i == 6 or i == 7:
270                 for indx, list in enumerate(N_r_list[0:9]):
271                     list[indx] *= cr_list800[indx][3]
272
273         sum_N_c = np.sum( [N_c1_june, N_c2_june, N_c3_june,
    N_c3_june, N_c4_june, N_c5_june, N_c6_june, N_c7_june,
274                           N_c8_june, N_c9_june, N_c10_june,
    N_c11_june, N_c12_june], axis=0)
275
276         amu = 6.022141E26  # kg to amu
277         plt.rcParams.update({'font.size': 12})
278         plt.rcParams['axes.labelsize'] = 12
279         plt.rcParams['axes.titlesize'] = 12
280         with sns.color_palette("colorblind", n_colors=13):
281
282             fig, (ax1) = plt.subplots(1, 1, sharey=True, sharex=
    True, figsize=(7, 6))
283             fig.tight_layout()
284
285             for indx, list in enumerate(N_c_list):
286                 ax1.plot(alt / 1e3, list[indx] / (1e4 * amu), label
    =f"{dust_sizes[indx]} nm")
287
288             ax1.plot(alt / 1e3, sum_N_c / 1e4, label=f"Total",
    color="black")
289
290             ax1.set_title("$v_r = 800m.s^{-1}$")
291             ax1.legend(loc="upper left")
292             ax1.grid(alpha=0.6)
293             ax1.tick_params(axis='x', labelsize=12)
294             ax1.tick_params(axis='y', labelsize=12)
295             ax1.set_yscale("log")
296             labelLines(ax1.get_lines(), zorder=2.5, xvals=[86],
    fontsize=10)
297             ax1.set_xlim(80, 95)
298             ax1.set_ylim(1e3, 1e12)
299             ax1.set_yticks([1e3, 1e5, 1e7, 1e9, 1e11])
300             ax1.set_ylabel("Mass per area [amu/cm$^2$]")
301             ax1.set_xlabel("Number density [#/cm$^3$]")
302             plt.tight_layout()
303             plt.savefig("C:/Users/Herma/PycharmProjects/
    Master_thesis/src/figures/results/Impacted_particles/test.
    png", format="png", bbox_inches='tight', dpi=300)
304             plt.show()
```